J. Fluid Mech. (2005), *vol.* 536, *pp.* 285–319.
doi:10.1017/S002211200500488X Printed in the United Kingdom

A numerical study of the influence of initial perturbations on the turbulent Rayleigh–Taylor instability

By P. RAMAPRABHU[1], GUY DIMONTE[1] AND M. J. ANDREWS[2]

[1]Los Alamos National Laboratory, Los Alamos, NM 87545, USA

[2]Department of Mechanical Engineering, Texas A&M University, College Station, TX 77843, USA

(Received 27 April 2004 and in revised form 21 February 2005)

The effect of initial conditions on the growth rate of turbulent Rayleigh–Taylor (RT) mixing has been studied using carefully formulated numerical simulations. A monotone integrated large-eddy simulation (MILES) using a finite-volume technique was employed to solve the three-dimensional incompressible Euler equations with numerical dissipation. The initial conditions were chosen to test the dependence of the RT growth coefficient (α_b) and the self-similar parameter ($\beta_b = \lambda_b/h_b$) on (i) the amplitude, (ii) the spectral shape, (iii) the longest wavelength imposed, and (iv) mode-coupling effects. With long wavelengths present in the initial conditions, α_b was found to increase logarithmically with the initial amplitudes, while β_b is less sensitive to amplitude variations. The simulations are in reasonable agreement with the predictions for α_b from a recently proposed model, but not for β_b. In the opposite limit where mode-coupling dominates, no such dependence on initial amplitudes is observed, and α_b takes a universal lower-bound value of $\sim 0.03 \pm 0.003$. This may explain the low values of α_b reported by most numerical simulations that are initialized with annular spectra of short-wavelength modes and hence evolve purely through mode-coupling. Small-scale effects such as molecular mixing and kinetic energy dissipation showed a weak dependence on the structure of initial conditions. Initial density spectra with amplitudes distributed as k^0, k^{-1} and k^{-2} were used to investigate the role of the spectral slopes on the development of turbulent RT mixing. Furthermore, in a separate study, the longest wavelength imposed in the initial wavepacket was also varied to determine its effect on α_b. It was found that the slopes of the initial spectra, and the longest wavelength imposed had little effect on the RT growth parameters.

1. Introduction

The Rayleigh–Taylor (RT) instability occurs when a light fluid (ρ_1) accelerates a heavy fluid (ρ_2) in the presence of infinitesimal perturbations at the interface. The instability is of interest to inertial confinement fusion (Lindl 1998), because it causes mixing of shell material into the deuterium fuel decreasing the thermonuclear yield. It is well-known (Chandrasekhar 1961) that for a single-mode perturbation with amplitude h_0 and wavelength $\lambda = 2\pi/k$ in the linear regime ($h \ll 1/k$), the amplitude grows exponentially according to:

$$h(t) = h_0 \cosh(\Gamma t) \tag{1}$$

where $\Gamma = \sqrt{Agk}$ is the classical growth rate, and the Atwood number $A = (\rho_2 - \rho_1)/(\rho_2 + \rho_1)$ is the non-dimensional parameter that characterizes the density contrast. At large amplitude ($h > 1/k$), nonlinearities reduce the growth rate and the amplitude increases only secularly in time. In this regime, the light fluid penetrates the heavy fluid as bubbles and the heavy fluid forms finger-like structures referred to as spikes. At small A, bubbles and spikes have the same penetration depths, while this symmetry is noticeably broken at higher density differences. The bubbles attain a terminal velocity given by (see for instance Gonchorov 2002)

$$v_b = c_\infty \sqrt{Ag\lambda_b/2}, \tag{2}$$

where the constant c_∞ can be interpreted as a Froude number. Three-dimensional bubbles are determined to have a value of $c_\infty \sim 0.5$ for $A = 1$ from single-mode studies of bubbles in cylindrical geometries (Layzer 1955; Alon *et al.* 1995; Gonchorov 2002; Sohn 2003 – potential theory models; Davies & Taylor 1950; Collins 1967 – experiments). The determination of c_∞ at arbitrary Atwood numbers is more complicated, and a detailed discussion of this and other effects is deferred until § 5. Thus, for single-mode with fixed λ, the nonlinear RT growth rate is independent of the initial amplitude.

In the presence of a spectrum of modes, the RT flow is dominated by successively longer wavelengths λ_b because they have a larger terminal bubble velocity v_b (equation (2)), given by:

$$\frac{\mathrm{d}h_b}{\mathrm{d}t} \propto \sqrt{\lambda_b}. \tag{3}$$

If the bubbles grow self-similarly, namely, they preserve their aspect ratio with constant $\lambda_b/h_b = \beta_b$. Equation (3) is then solved by:

$$h_b = \alpha_b A g t^2, \tag{4}$$

where α_b is the RT growth constant associated with bubbles. Physically, self-similarity could be achieved in two ways:

(i) bubble merger: the nonlinear coupling of two or more bubbles to form a larger structure;

(ii) bubble competition: the growth and saturation of modes present in the initial perturbations.

The first process involves the nonlinear coupling of saturated modes ($h \sim 1/k$) and, thus, may produce a universal α_b (Glimm & Li 1988; Alon *et al.* 1995). The second process depends on the initial conditions, albeit weakly since the initial growth is exponential.

Birkhoff (1955) was the first to propose (4) based on a model for the competition of individual modes to characterize the dependence of α_b on the initial amplitudes for two-dimensional flows. Birkhoff matched the velocity in the linear regime (obtained from (1)) with the nonlinear terminal velocity (2) when $h_k \sim 1/k$, thus relating the nonlinear amplitude of a mode to its initial magnitude – this technique is referred to as the Fermi transition (Layzer 1955). Birkhoff's model predicts a dependence of α_b on three parameters, namely, the initial amplitude of fluctuations h_{0k}, the Froude number Fr, and the threshold for the nonlinear transition ($\sigma \sim h_k k$). However, he assumed fixed values for Fr, σ and h_{0k} giving him a value for $\alpha_b = 0.06$. Cherfils & Mikaelian (1996) generalized Birkhoff's model to arbitrary initial amplitudes, and a

nonlinear threshold σ, giving for α_b, at $A = 1$,

$$\alpha_b = \frac{Fr}{4\left[(2\pi)^{-1/2}\ln(\sigma/h_{0k}) - \sigma/Fr\right]}. \tag{5}$$

Birkhoff's model further suggests that for self-similarity (i.e. α_b is time-independent) to be established, the initial one-dimensional spectra should have amplitudes that vary according to k^{-1} in the above equation.

One difficulty with Birkhoff's model is that it considers only individual modes in a bubblefront that do not interact with their neighbours, whereas Haan (1989) postulated that adjacent modes in a wavepacket interfere constructively, so that the Fermi-transition occurs when the quadrature sum of modal amplitudes in the wavepacket is $\sim\sigma/k$. Thus, individual modes may become nonlinear even when their amplitudes are below the threshold owing to their interaction with adjacent modes. Such a picture was very successful in relating the nonlinear saturation of the beam-plasma instability for a single mode to the multi-mode case (DeNeef 1975; Dimonte 1982).

Dimonte (2004) combined the ideas of Birkhoff and Haan by applying the Fermi transition to a self-interacting wavepacket in three-dimensions. The resulting model equations are re-derived in the Appendix and summarized below:

$$\alpha_b = \frac{C\sqrt{\pi}}{4}\left[\ln\left(\frac{2C\sqrt{\pi}}{k\langle h_{0k}\rangle}\right) - 1\right]^{-1}, \tag{6}$$

$$\beta_b = \frac{2\sqrt{\pi}}{C}\left[\ln\left(\frac{2C\sqrt{\pi}}{k\langle h_{0k}\rangle}\right) - 1\right]^{-1}. \tag{7}$$

We can interpret (4) to be the quadratic envelope of the growth curves of all such individual modes (see figure 4 of Dimonte 2004). Equations (6) and (7) then suggest that by changing the initial amplitudes, we may cause them to saturate earlier (or later) and, thus, the quadratic coefficient of this envelope (α_b) can be changed. Since the disturbances grow exponentially up to saturation, the time to nonlinearity (and thus α_b) depends logarithmically on the initial amplitudes. Here, $k\langle h_{0k}\rangle$ is the non-dimensional initial amplitude with k chosen to be the dominant wavenumber in the initial spectrum, and $\langle h_{0k}\rangle$ is the root mean square (r.m.s) of fluctuations computed over a wavepacket of width δk (estimated in the Appendix). Thus,

$$\langle h_k\rangle = \left[\frac{L^2}{2\pi}\int_{k-\delta k}^{k+\delta k} h_{k'}^2 k'\,\mathrm{d}k'\right]^{1/2}. \tag{8}$$

In (6) and (7), C is a modified Froude number defined as:

$$C = Fr\sqrt{\frac{2}{1+A}\frac{D_b}{\lambda}}, \tag{9}$$

to accommodate ambiguities in the definition of a bubble wavelength and is further discussed in § 5. From the above, it follows that for a spectral structure with $h_k \sim k^{-2}$, equation (8) gives for $k\langle h_{0k}\rangle$ a constant value independent of k. Consequently, as the flow samples longer wavelengths, (6) and (7) produce a time-independent value of α_b and β_b, resulting in self-similarity. Inagamov (1978) was the first to point out that a k^{-2} initial spectrum is required for self-similarity in RT flows. This is equivalent to requiring $h_{0k} \sim k^{-1}$ for two-dimensional flows (Birkhoff's model).

The implication of (4) is that the flow has lost memory of the initial conditions and the only remaining independent length scale is the effective acceleration distance

Agt^2. However, a universal value for the growth constant α_b has eluded both experimental and numerical investigations. While experiments report higher values for α_b of 0.05–0.07 (Dalziel 1993; Dimonte & Schneider 2000; Read 1984; Snider & Andrews 1994; Linden, Redondo & Youngs 1993), numerical simulations have often found lower values of 0.02–0.03 (Youngs 1989 (two-dimensional) 1991, 1994, 2003; Cook & Dimotakis 2001; Young *et al.* 2001; Dimonte *et al.* 2004). Simulations suffer from significant numerical diffusion, which could also contribute to the reduction in the value of α_b. However, we argue in the following that these differences may be due to variations in the structure and magnitude of the initial perturbations.

This analysis assumes the presence of long-wavelength perturbations in the initial spectral content whose amplitudes govern their late-time self-similar growth. In the opposite limit, where low-wavenumber modes have negligible energy compared with the high-wavenumber content, long-wavelengths in the flow are generated largely by the nonlinear coupling (Dimonte *et al.* 2004; Haan 1991) of modes (a process insensitive to the initial conditions). The resulting evolution of bubble amplitudes is thus independent of the initial conditions, and α_b takes up a universal, lower bound value of $\sim 0.03 \pm 0.003$ (Dimonte *et al.* 2004).

Youngs (2003) performed large-eddy simulations (LES) of RT instability at a resolution of $720 \times 480 \times 480$, initialized with a spectrum that had energy only in the high mode numbers (90–180). The resulting flow evolved with a growth rate of $\alpha_b \sim 0.027$, which doubled to $\alpha_b \sim 0.057$ with the addition of a single long wavelength in the initial spectrum at a mode number of 2. Cook & Dimotakis (2001) in their direct numerical simulations (DNS) of RT instability at a Reynolds number of ~ 3000 (defined as $Re = h\dot{h}/\nu$), studied the effect of the initial spectral peak (at $k = k_{max}$) on the growth rate. However, they report self-similarity only for the case with the highest value of the peak wavenumber k_{max}. Again, their plots of α_b show a lower value than that obtained from experiments. We also note the DNS of Young *et al.* (2001) employed an initial annular spectrum that evolves through mode-coupling, giving $\alpha_b \sim 0.03$. Simulations in which numerical diffusion is suppressed through a front-tracking technique (Glimm *et al.* 2001) have found a higher value for $\alpha_b \sim 0.07$. The effects of numerical diffusion are discussed in § 4. Dalziel, Linden & Youngs (1999) modelled the experimentally observed initial conditions in their three-dimensional numerical simulations and obtained good agreement in both the large- and small-scale features of the flow. They found that while global features such as α_b depended on the presence of long wavelengths in their initial conditions, small-scale features such as the level of molecular mixing did not. Kadau *et al.* (2004) summarize molecular dynamics simulations that obtain $\alpha_b \sim 0.05$, but did not include a detailed characterization of the initial conditions. The simulations were initialized with thermal fluctuations, which were not varied to study the resulting α_b behaviour. Figure 1 is a summary of experimental and numerical values of α from published results from codes over the period 1991–2004. Note that the higher values of α from numerical simulations shown in figure 1 were obtained from the front-tracking simulations.

In this paper, we examine both the bubble-merger and bubble-competition limits through three-dimensional numerical simulations with carefully imposed initial perturbations. We explore the bubble competion limit with simulations initialized with long wavelengths at different amplitudes. We also study the bubble merger limit with simulations with annular spectra at different amplitudes for initial conditions. In addition, other possible influences on the growth rate, such as the spectral shapes (referred to as the spectral index (SI) herein, and quantified as the exponent of the wavenuumber, i.e. $h_{0k} = k^{S.I.}$), and the longest wavelength imposed are investigated here.

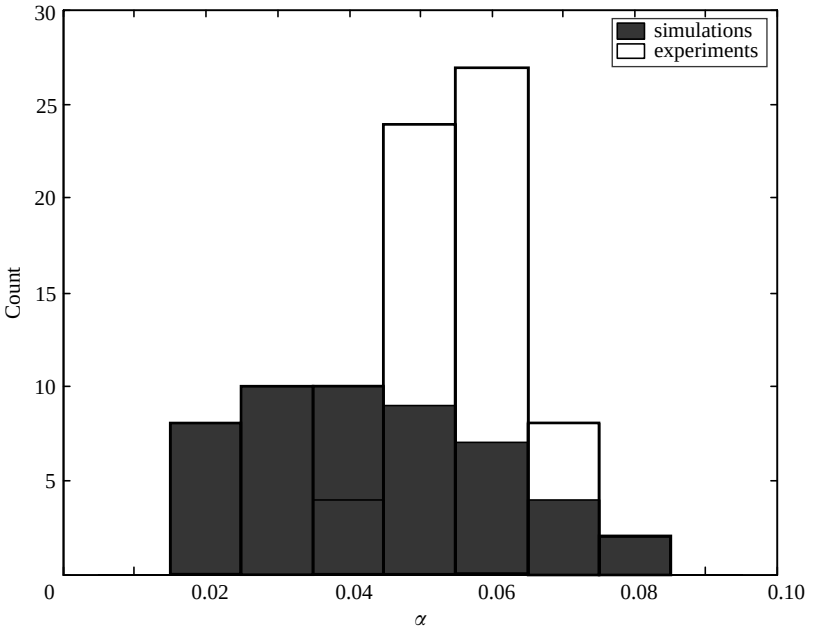

FIGURE 1. Histogram of RT growth constant α from simulations and experiments.

The rest of the paper is organized as follows. In the next section, we describe the numerical algorithm, and details of the computational set-up. Section 3 is a description of the problem set-up and parameters. Results from a single-mode study to determine the numerical viscosity of the computational scheme are summarized in § 4, and the multi-mode studies are described in § 5. The conclusions are discussed in § 6.

2. Numerics

A three-dimensional third-order accurate finite-volume program *RTI-3D*, developed by Andrews (1995), was used to solve the Euler equations. The non-Bousinesq governing equations are

$$\text{continuity}: \frac{\partial(f_i\rho_i)}{\partial t} + \frac{\partial(f_i\rho_i u)}{\partial x} + \frac{\partial(f_i\rho_i v)}{\partial y} + \frac{\partial(f_i\rho_i w)}{\partial z} = 0, \tag{10a}$$

$$\boldsymbol{x}\text{-momentum}: \frac{\partial(f_i\rho_i u)}{\partial t} + \frac{\partial(f_i\rho_i u^2)}{\partial x} + \frac{\partial(f_i\rho_i uv)}{\partial y} + \frac{\partial(f_i\rho_i uw)}{\partial z} = -f_i\frac{\partial p}{\partial x} + f_i B_{i,x}, \tag{10b}$$

$$\boldsymbol{y}\text{-momentum}: \frac{\partial(f_i\rho_i v)}{\partial t} + \frac{\partial(f_i\rho_i uv)}{\partial x} + \frac{\partial(f_i\rho_i v^2)}{\partial y} + \frac{\partial(f_i\rho_i vw)}{\partial z} = -f_i\frac{\partial p}{\partial y} + f_i B_{i,y}, \tag{10c}$$

$$\boldsymbol{z}\text{-momentum}: \frac{\partial(f_i\rho_i w)}{\partial t} + \frac{\partial(f_i\rho_i uw)}{\partial x} + \frac{\partial(f_i\rho_i vw)}{\partial y} + \frac{\partial(f_i\rho_i w^2)}{\partial z} = -f_i\frac{\partial p}{\partial z} + f_i B_{i,z}, \tag{10d}$$

where the f_is are the volume fractions of the ith fluid ($f_1 + f_2 = 1$); u, v, and w are the velocities in the x-, y- and z-directions, respectively; and $B_{i,(x,y,z)}$ is a body force term (buoyancy). To avoid check-boarding of the pressure field, a staggered

cell arrangement is used for the pressure and velocities, with the pressure node located at the cell centre, while the velocities are computed at the cell faces. Explicit timestepping was used in the solution of these equations, with the size of the time step chosen to satisfy a Courant condition. A three-stage fractional step algorithm is used to advance the solution in time. At each step, an advection calculation followed by a Langrangian source term update is performed. In the Lagrangian calculation, intermediate velocities are obtained as

$$u_E^* = u_E^{n+1/2} + \frac{\Delta t}{\rho_i \Delta x}\left(p_P^n - p_E^n\right) + g_x, \tag{11a}$$

$$v_E^* = v_E^{n+1/2} + \frac{\Delta t}{\rho_i \Delta y}\left(p_P^n - p_N^n\right) + g_y, \tag{11b}$$

$$w_T^* = w_T^{n+1/2} + \frac{\Delta t}{\rho \Delta z}\left(p_P^n - p_T^n\right) + g_z, \tag{11c}$$

where E, N and T are the east, north and top cell faces, and $g_x = g_y = 0$. The superscript $n+1/2$ denotes an intermediate value obtained after the advection update, and the asterisk represents the results of the Lagrangian update. To satisfy continuity, the net mass flux across each cell is set to zero:

$$\delta V_E - \delta V_W - \delta V_N - \delta V_S - \delta V_T - \delta V_B = 0, \tag{12}$$

where, for example, $\delta V_E = \Delta t \Delta y \Delta z (u_E^{n+1} \rho_E^{n+1})$. Here, $n+1$ indicates updated velocities that satisfy continuity, after a correction has been added so that $u_E^{n+1} = u_E^* + \Delta u_E$ for velocities and $p_P^{n+1} = p_P^* + \Delta p_E$ for pressure, where P represents the cell-centred pressure node. Substituting the updated velocities into (11) and subtracting (11) evaluated with the velocities at *, we get for the east-face velocity,

$$\Delta u_E = \frac{\Delta t}{\rho_i \Delta x}(\Delta p_P - \Delta p_E), \tag{13}$$

with similar expressions for the other components. Using these expressions in (12) results in a Poisson equation for the pressure correction Δp.

$$-a_P \Delta p + a_E \Delta P_E + a_W \Delta P_W + a_N \Delta P_N + a_S \Delta P_S + a_T \Delta P_T + a_B \Delta P_B = -D, \tag{14}$$

where, for instance,

$$a_E = -\frac{\Delta t \Delta y \Delta z}{\Delta x}\left(\frac{f_{1,E}^{n+1}}{\rho_1} + \frac{f_{2,E}^{n+1}}{\rho_2}\right). \tag{15}$$

An iterative conjugate gradient algorithm is used to solve the Poisson equation. The iterative procedure is repeated until the residual $|D|$ in (14) summed over all the cells is less than some specified threshold ($= 10^{-4}$). Note that this is essentially the pressure correction method popularized in the SIMPLE method (Patankar 1972). The solution of (14) takes up most of the computational effort.

Of significant importance in the simulation of RT flows is the convection calculation of the fluxes of mass and momentum. A third-order Van Leer method (Van Leer 1977) was used to compute convective fluxes that minimizes numerical diffusion and prevents spurious overshoots and undershoots, which occur because of the use of higher-order numerical schemes. A two-phase, two-dimensional version of this code was tested and validated for both RT and Kelvin–Helmholtz flows by Andrews (1995). The three-dimensional single-phase version was used in Dimonte *et al.* (2004) to compute both the single- and multi-mode RT problems, and it compared well with other benchmark codes commonly used. While there is no specified physical viscosity, numerical

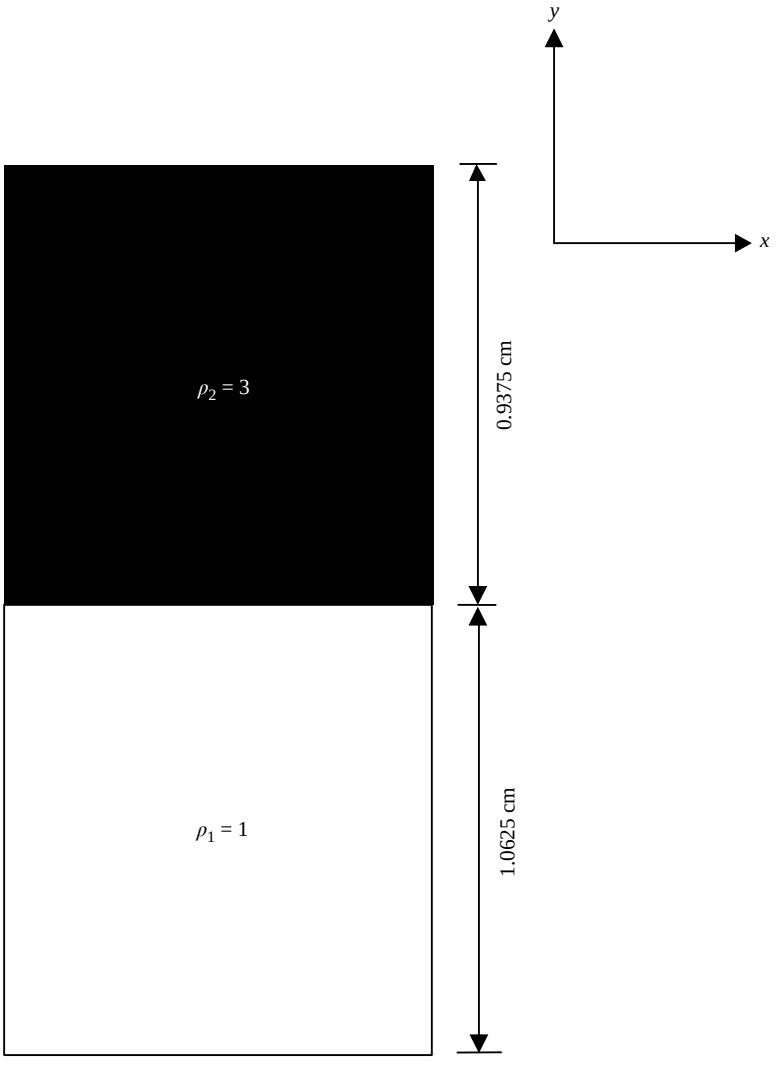

FIGURE 2. Two-dimensional slice of computational domain used in numerical simulations: $\rho_1 = 1\,\mathrm{g\,cm^{-3}}$, and $\rho_2 = 3\,\mathrm{g\,cm^{-3}}$.

diffusion damps out small scales in much the same manner as molecular diffusion. Such schemes belong to the class of algorithms known as monotone integrated large-eddy simulation (MILES) techniques and have been shown to be effective in the solution of flows with shocks and discontinuities such as RT and Richtmeyer–Meshkov instabilities (Youngs 2003). In § 5, we investigate the role of this effective viscosity in the present numerical solution method, in the context of the MILES approach.

3. Problem set-up

Figure 2 is a schematic of our computational domain. The dimensions of the three-dimensional box are $1\,\mathrm{cm} \times 1\,\mathrm{cm} \times 2\,\mathrm{cm}$ in the x-, y- and z-directions, respectively (where z- is the direction of gravity). The interface between the heavy (ρ_2) and light (ρ_1) fluids is at $z = 0$. The densities were chosen to be $\rho_1 = 1$ and $\rho_2 = 3\,\mathrm{g\,cm^{-3}}$ ($A = 0.5$), while the acceleration due to gravity g_z was set to be $0.3183\,\mathrm{cm\,s^{-2}}$. The box

is 0.9375 cm in the positive z-direction and 1.0625 cm in the negative z-direction to account for the slightly different growth rates of bubbles and spikes at this Atwood number. Perturbations ($h_0(x, y)$) are imposed at the interface ($z = 0$) as fluctuations of a constant density surface. These are then converted to volume fraction fluctuations using, $f_1(x, y) = 1 + h_0(x, y)/\Delta$ for $h_0 < 0$, and $f_1(x, y) = h_0(x, y)/\Delta$ for $h_0 > 0$, where Δ is the zone width. The pressure is initialized to the hydrostatic value in this incompressible problem using $p(z) = -\int \rho g \, dz$, where $\rho = f_1\rho_1 + f_2\rho_2$ is the unperturbed initial density field. This is an important initial condition to set, because without it the algorithm will seek to establish the hydrostatic condition on the first time step, involving hundreds, if not thousands, of iterations for the pressure correction calculation. If an initial hydrostatic pressure field is provided, only three or four iterations are required on the first time step for pressure convergence. Periodic boundary conditions were used in the x- and y-directions, while zero-flux conditions were imposed in the z-direction. All the simulations reported here used a resolution of $128 \times 128 \times 256$ grid points in the x-, y- and z-directions, respectively. The calculations were stopped when the bubble height reached ~ 0.8 cm to avoid boundary effects. Bubble and spike amplitudes (defined below) were written out at each time step, while three-dimensional data files containing the volume fractions and velocities were written for $Agt^2 = 1, 2, 3 \ldots$ The simulations were executed on a SGI Origin 3000 machine at Texas A&M University. The run-times averaged around 800 CPU hours per calculation. Each of these simulations required 1 GB of RAM and 6 GB of storage.

4. Single-mode dynamics – MILES evaluation

While *RTI-3D* solves the Euler equations with no explicitly specified viscosity, numerical diffusion serves to dissipate small scales. Such numerical techniques (MILES) have been demonstrated to be particularly attractive for flows with shocks (Richtmeyer–Meshkov) and discontinuities (RT) (Youngs 2003). We model the dissipation with an effective viscosity by calibrating small-amplitude single-mode simulations with linear theory results (Chandrasekhar 1961). The technique is described in detail in Dimonte *et al.* (2004), and some essential aspects are reviewed herein. The single-mode calculations were initialized with perturbations in the x- and y-directions with a wavelength $\lambda = 1$ cm and amplitude $a_0 = 0.001$ cm, given by

$$h_0(x, y) = a_0\left(\cos\left(\frac{2\pi x}{\lambda}\right) + \cos\left(\frac{2\pi y}{\lambda}\right)\right). \tag{16}$$

The density interface at the centreline was converted to fluctuations of volume-fraction as described in § 3. The calculations were performed at resolutions of $\lambda/\Delta = 4, 8, 16,$ and 32, where Δ is the zone width. In the presence of viscosity (physical or artificial), the exponential growth rate Γ of a small-amplitude RT mode k can be approximated by the following dispersion relation (Robinson & Swegle 1989):

$$\Gamma^2 = Akg - 4\nu k^2\Gamma + 4k^4\nu^2(\sqrt{1 + \Gamma/k^2\nu} - 1). \tag{17}$$

The viscosity, ν, is inferred by using the modified growth rate Γ from the numerical simulations (Dimonte *et al.* 2004). Here, Γ is obtained by fitting the observed amplitudes to linear theory ($h_k(t) = h_{0k}\cosh(\Gamma t)$). For the maximum resolution of $k\Delta = 0.196$ (32 zones/λ), it was found that (Dimonte *et al.* 2004) the growth rate approaches the inviscid value (i.e. $\Gamma/\sqrt{Akg} \sim 1$). At a resolution of 4 zones/λ, Γ is only $\sim 65\,\%$ of the inviscid value. From our results, we concluded that to resolve an RT mode completely, at least 8 nodes are required. As we will see in § 5, the implication of a numerical

Simulation	Spectral index (*S.I.*)	N_{min}	$k\langle h_{0k}\rangle$
1	−2	1	1.1×10^{-6}
2	−2	1	1.1×10^{-5}
3	−2	1	1.1×10^{-4}
4	−2	1	0.0011
5	−2	1	0.0044
6	−2	1	0.011
7	−2	1	0.044
8	−2	2	3.0×10^{-6}
9	−2	2	0.0003
10	−2	2	0.0044
11	−2	3	4.0×10^{-5}
12	−2	3	0.004
13	−2	3	0.04
14	−1	2	0.0045*
15	0	2	0.004*
16		16	4.7×10^{-6}*
17		16	4.7×10^{-4}*
18		16	0.047*

TABLE 1. List of simulations.

viscosity for multi-mode simulations is similar to that of a physical viscosity, as it sets an upper bound for the fastest growing modes. Smaller wavelengths, present in the initial conditions, or generated through nonlinear interactions (mode-coupling), are smeared out by the numerical viscosity. A similar analysis was performed for the nonlinear phase of single-wavelength bubble evolution. The $k\Delta = 0.196$ case gave a Froude number of ~ 0.6 (obtained by tracking the bubbletip), which is in good agreement with the value of 0.56 for a square periodic lattice of bubbles (Li, Jin & Glimm 1996). Since bubble velocities converged faster in the nonlinear stage, the more stringent resolution criterion of 8 zones/λ, obtained from the analysis of the linear stage, was adopted.

5. Multimode calculations

5.1. *Initial conditions*

Multimode calculations were designed to test the dependence of the growth constant α_b on the initial amplitudes, spectral index, mode-coupling and longest imposed wavelength. The perturbations $h_0(x, y)$ are initialized as a superposition of up to 32 modes, and expressed as

$$h_0(x, y) = \sum_{k_x, k_y} a_k \cos(k_x x)\cos(k_y y) + b_k \cos(k_x x)\sin(k_y y) + c_k \sin(k_x x)\cos(k_y y) + d_k \sin(k_x x)\sin(k_y y), \quad (18)$$

where $k = \sqrt{k_x^2 + k_y^2}$. In the above, both the modal amplitudes a_k, b_k, etc. and the phases are assigned randomly. Table 1 gives all the calculations. Simulations 1–13 were initialized with $k\langle h_{0k}\rangle$ ranging from 1.1×10^{-6} (case 1) to 0.044 (case 13). All these cases had a_k, b_k, c_k, and d_k varying as k^{-2} to verify (6) and (7), and thus constitute a study of the initial amplitudes. These calculations had energy in mode numbers ($n = kL/2\pi$) 1–32 (for cases 1–7), 2–32 (for cases 8–10), and 3–32 (for cases 11–13). Cases 5, 10 and

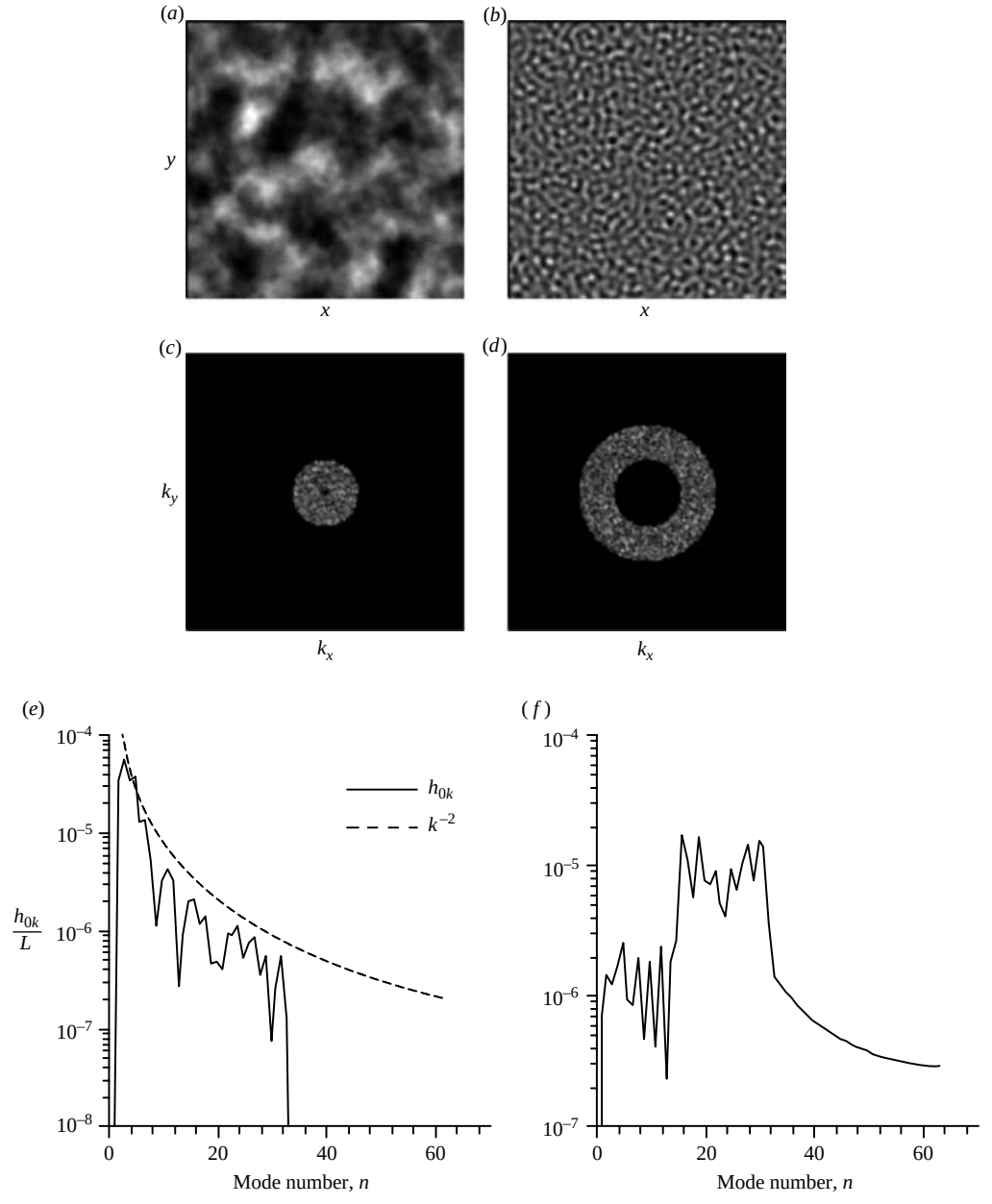

FIGURE 3. Initial perturbations for simulation 10 in (*a*) physical, (*c*) wavenumber space, and (*e*) azimuthally averaged in wavenumber space. Initial perturbations for simulation 18 in (*b*) physical, (*d*) wavenumber space, and (*f*) azimuthally averaged in wave number space.

12 were initialized with the same amplitudes ($k\langle h_{0k}\rangle = 0.004$), but with their smallest mode numbers varying as $N_{min} = 1$, 2 and 3, respectively, and constitute a study of the effect of the longest wavelength imposed. Similarly, the role of spectral shapes was studied by initializing cases 10, 14 and 15 with the same amplitude ($k\langle h_{0k}\rangle = 0.0044$) and N_{min} (= 2), but spectral indices (SI) of $-2, -1$ and 0 (white noise), respectively. Figures 3(*a*) and 3(*c*) are the perturbation amplitudes for a typical case (case 10)

in physical and wavenumber space, respectively. Figure 3(*e*) is the corresponding azimuthally averaged Fourier amplitudes revealing the k^{-2} (dashed line) structure of the spectra. To test the opposite limit of mode-coupling, the perturbation energy was confined to an annulus ($16 < n < 32$) in wavenumber space (see figures 3*b* and 3*d*) for cases 16, 17 and 18, with amplitudes of 4.7×10^{-6}, 4.7×10^{-4} and 4.7×10^{-2}, respectively. The azimuthally averaged Fourier amplitudes for case 18 are shown in figure 3(*f*). Most numerical simulations of RT instability (Youngs 1991, 1994, 2003; Cook & Dimotakis 2001; Young *et al.* 2001) are initialized with similar annular distributions. It is expected that the mode-coupling cases will produce a much lower growth rate than the simulations initialized with the longer modes (Dimonte *et al.* 2004), because the long wavelengths dominate the flow at late time. It must also be noted that most experiments have long-wavelength content in their initial conditions (Dimonte & Schneider 2000; Ramaprabhu & Andrews 2004), which could explain the higher values of α typically reported from such studies. The following is a quick reference for all cases reported in this work:

(*a*) Initial amplitude study: cases 1–13.
(*b*) Spectral Index study: cases 10, 14 and 15.
(*c*) Mode coupling study: cases 16–18.
(*d*) Longest wavelength study: cases 5, 10 and 12.

We now address the issue of the most dominant wavenumber (i.e. having the largest linear growth rate) in the presence of numerical viscosity in these simulations. Numerical viscosity (like other stabilizing mechanisms, such as surface tension) places an upper bound on the fastest growing wavenumber. Setting $\partial \Gamma / \partial k = 0$ in (17), the peak growth rate $\sim 0.4(g^2/\nu)^{1/3}$ (Miles & Dienes 1966; Robinson & Swegle 1989) occurs at the wavenumber

$$k_p \approx 0.5 \left(\frac{Ag}{\nu^2} \right)^{1/3}. \tag{19}$$

For the current simulations, the fastest growing mode number was determined to be $N_p \sim 24$ (Dimonte *et al.* 2004), and within the present range of modes imposed in the initial conditions. This guarantees that the linear growth stage is reproduced accurately by these calculations.

Figure 4(*a*) shows the evolution of the bubble and spike amplitudes (h_b and h_s) as a function of the self-similar length Agt^2 (cm) for case 10. The bubble and spike amplitudes are defined as the z-location where the average value (over the (x, y)-plane) of f_1 reaches 1 % and 99 %, respectively. We assume that nonlinearity sets in when the most dominant wavelength $\lambda_p = 2\pi/k_p$ saturates. The time at which this transition occurs may be determined by equating the linear and nonlinear velocities of a mode evaluated at a transition time t_k, using the so-called Fermi transition (see Appendix), giving

$$t_k = (Ak_p g)^{-1/2} \cosh^{-1} \left(\frac{2C\sqrt{\pi}}{k \langle h_{0k} \rangle} \right). \tag{20}$$

For the parameters used here, the transition occurs at $Agt^2 \sim 0.604$ for case 10. Table 2 gives the transition times from all the simulations. The statistics for each case were determined after the nonlinear transition had set in. One concern when computing α_b and β_b was that it had to be done in a time window after the nonlinear transition, but before the emergence through mode-coupling of longer wavelengths not originally imposed. The time t_{mc} at which wavelengths due to mode-coupling are longer than the longest wavelength present in the initial conditions is determined as follows. From

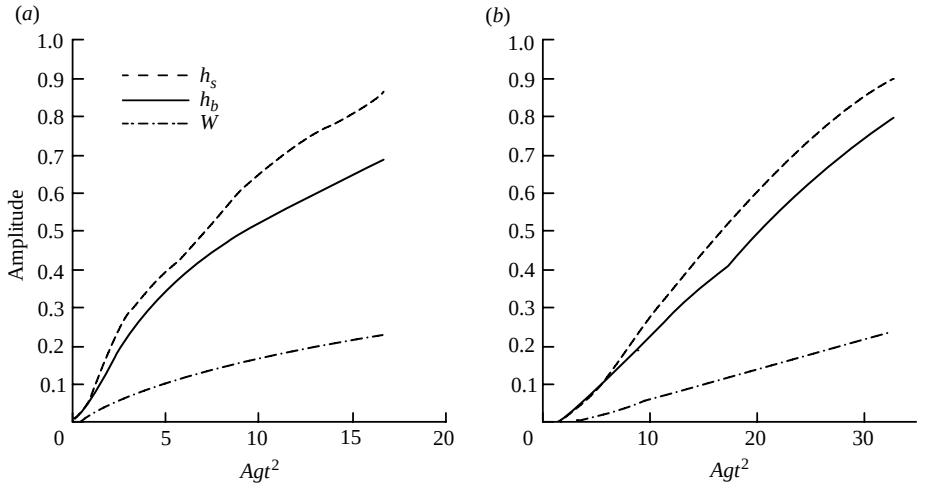

FIGURE 4. Evolution of bubble and spike amplitudes (h_b and h_s), and integral width W for (a) case 10 ($N_{min} = 2$) and (b) case 1 ($N_{min} = 1$).

Simulation	Transition time Agt_k^2	Mode-coupling onset time, $A_t g t_{mc}^2$
1	3.52	–
2	2.44	–
3	1.55	–
4	0.87	–
5	0.55	–
6	0.41	–
7	0.18	–
8	2.89	33
9	1.25	20
10	0.60	15
11	1.81	18
12	0.58	8
13	0.22	6
14	1.15	18
15	0.62	16
16	3.70	–
17	1.14	–
18	0.23	–

TABLE 2. The nonlinear transition time t_k for the 17 simulations.

the estimated width of the wavepacket $\delta k = \pm 3k_p/8$ (see Appendix), where k_p is the dominant mode at any given time, we determined the longest wavelength in the computational domain to be

$$k_{min} = k_p - \tfrac{3}{8}k_p. \tag{21}$$

Thus, when k_p is the dominant mode, k_{min} has just saturated. When k_{min} is less than the lowest mode number imposed in the initial conditions, mode-coupling effects are said to be significant. For example, for simulation 1 this would occur when n_{min} dropped below a value of 3. Thus, the cutoff time is chosen as the value of t, when $k_p = 8k_{min}/5$. The dominant mode k_p at any time is determined from the bubblefront

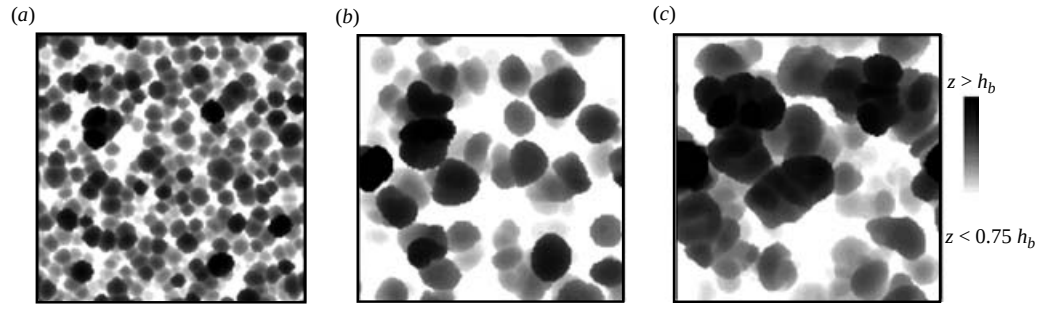

FIGURE 5. Bubble fronts $Z_b(x, y)$ from simulation 10 at early-, mid- and late times ((*a*) $Agt^2 = 2$, (*b*) 8 and (*c*) 16).

image by an autocorrelation procedure described below. The values of α_b and β_b, and other quantities, are then obtained by averaging for $t_k \leqslant t \leqslant t_{mc}$. Table 2 also the mode-coupling transition times from the calculation. For the simulations initialized with $N_{min} = 1$, the transition to pure mode-coupling dominance never occurs. For cases with low-amplitude initial perturbations, the products of mode-coupling may play a greater role in the dynamics owing to their increased relative significance. This is discussed in detail in § 5. Thus, it is challenging to completely isolate the contributions of mode-coupling and long-wavelength saturation in such studies.

The ratio $h_s/h_b \sim 1.25$ observed in figure 4(*a*) at late time is consistent with experimental observations for $A \sim 0.5$ (Dimonte & Schneider 2000). (Their power-law dependence for the ratio of spike to bubble amplitudes

$$\frac{h_s}{h_b} = \left(\frac{\rho_2}{\rho_1}\right)^{0.33}, \tag{22}$$

gives a value of ~ 1.4 at these density ratios). We also plot the integral mix width defined as (Andrews & Spalding 1990)

$$W = \int \langle f_1 \rangle \langle f_2 \rangle \, \mathrm{d}z. \tag{23}$$

For small Atwood numbers $h_b \sim h_s$, assuming a linear profile for the volume fractions, $h \sim 3W$ consistent with figure 4(*a*) ($h \sim 3.2W$ if the effects of numerical diffusion are considered – Youngs 2003) – Andrews & Spalding (1990) use a multiplicative factor of 6 in (23) to relate W directly to the total mix width. It is not clear why a second transition in the h_b and h_s time traces is observed around $Agt^2 \sim 5$. We initially suspected this behaviour might be due to the lack of sufficient bubbles/spikes required for convergent statistics. To resolve this, h_s and h_b were also computed from the x-intercept of a linear fit to the volume fraction profiles (see Youngs 1989; Schneider, Dimonte & Remington 1998). Since this method (which is less susceptible to statistical fluctuations) yielded the same α_b (within $\pm 10\,\%$) as the plots in figure 4(*a*), the 1 % and 99 % thresholds have been used throughout this paper. Another possible reason for the transition might be the emergence of products of mode-coupling around that time. Indeed, no such transition is observed for cases initialized with $N_{min} = 1$ (figure 4*b*), since the mode-coupling products in these cases never exceed $N_{min} = 1$. Thus, for cases with $N_{min} = 2, 3$, the bubble statistics were computed for $t_k < t < t_{mc}$.

Figure 5 shows the bubblefronts $Z_b(x, y)$ (defined as iso-surfaces of $f_1 = 0.01$) at three stages of the RT evolution ($Agt^2 = 2, 8$ and 16) for case 10. Only the bubblefronts with $Z_b > 0.75h_b$ (i.e. the leading bubbles) are visualized in figure 5.

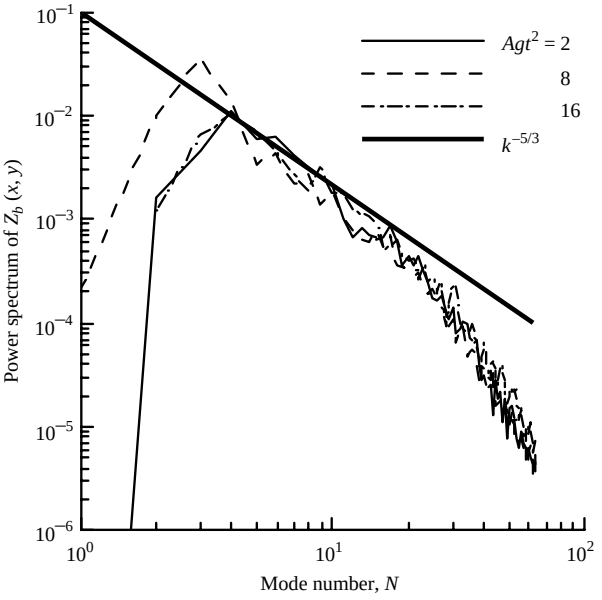

FIGURE 6. Azimuthally averaged power spectra of bubble fronts $Z_b(x, y)$ from simulation 10 at early-, mid- and late times ($Agt^2 = 2$, 8 and 16).

There are ~ 120 bubbles at $Agt^2 = 2$, that coalesce to ~ 9 large bubbles by the end of the calculation. This corresponds to about $\log_2(120/9) \sim 3.7$ generations of bubble evolution. It is evident that even at $Agt^2 = 16$, the bubbles do not approach the box dimension $L = 1$ cm. Thus, we may assume that the flow is not affected by the boundaries throughout the calculation. The radial autospectra $E_{Zb}(k)$ of the bubble front function Z_b (x, y) is defined to ensure

$$\int_0^\infty E_{zb}(k)\,\mathrm{d}k = \langle Z_b^2 \rangle - \langle Z_b \rangle^2, \tag{24}$$

where $\langle \bullet \rangle$ denotes averaging over the (x, y)-plane. The radial autospectra was obtained by azimuthally averaging the two-dimensional power spectra of $Z_b(x, y)$ rotated through 30 angles. The results are plotted in figure 6 for $Agt^2 = 2$, 8 and 16. There is no dissipative range in these spectra owing to the absence of small-scale information in the definition of $Z_b(x, y)$. Consistent with the emergence of large-scale structures at late-time, the spectral peak shows movement towards lower mode numbers. However, at $Agt^2 \sim 2$, the spectral peak is at $N \sim 4$, which is higher than the imposed value of $N_{min} = 2$ for this case. We attribute this to wavenumber modulation effects owing to the presence of different size bubbles. To determine quantities, such as the Froude number and the self-similar parameter β_b, it is necessary to estimate the diameters of the dominant RT bubbles without such modulation effects. Thus, we use an autocorrelation-based technique (developed in Dimonte *et al.* (2004) and briefly reviewed next) to determine the average bubble diameters at different Agt^2.

The two-dimensional non-dimensional, autocorrelation function $\eta(x, y)$ of the bubble front $Z_b(x, y)$ is defined as

$$\eta(x, y) = \frac{\sum (Z_b(x', y') - \langle Z_b \rangle)(Z_b(x' + x, y' + y) - \langle Z_b \rangle)}{\sum (Z_b(x', y') - \langle Z_b \rangle^2)}, \tag{25}$$

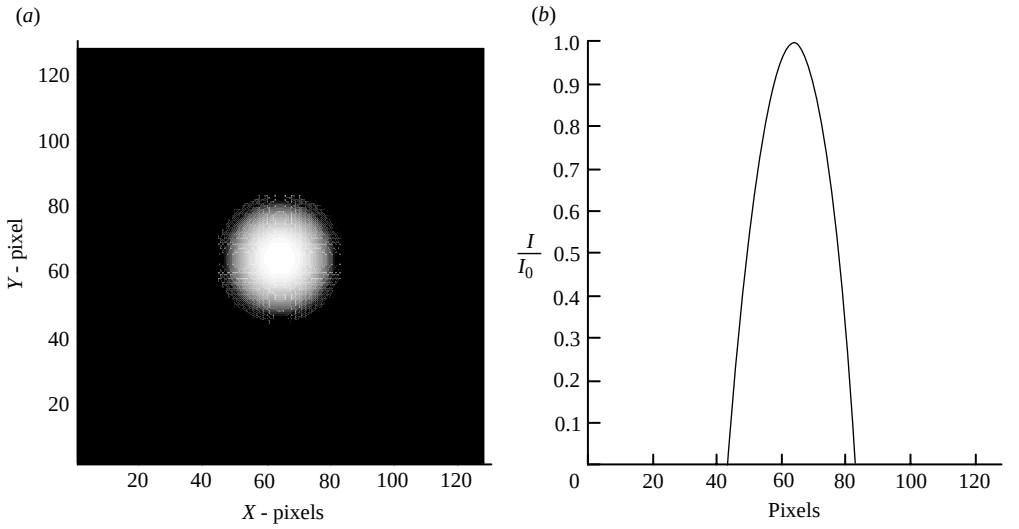

FIGURE 7. (*a*) Test image of radius 20 pixels with a parabolic (*b*) intensity profile. I_0 is the peak intensity value at the centre of the image.

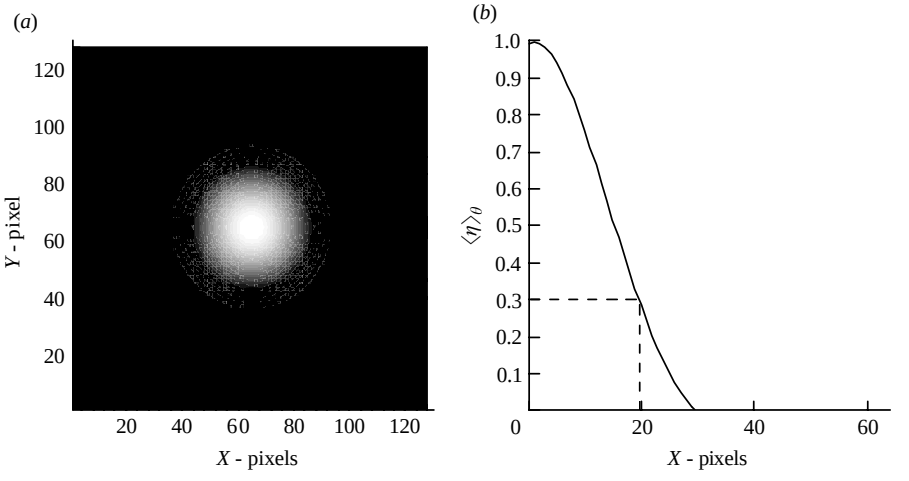

FIGURE 8. (*a*) Autocorrelation contours of test image from 6 (*a*) and the azimuthally averaged radial profile (*b*) showing a radius of ~ 20 pixels.

where the summations are over $0 \leqslant x', y' \leqslant L$. The azimuthal average $\langle \eta \rangle_\theta$ is obtained by averaging $\eta(x, y)$ rotated through 24 angles. This technique was applied to test images with objects of known diameters, and it was found that the radial location where $\langle \eta \rangle_\theta$ dropped to a value of 0.3 corresponded to the mean radius of the test objects. Figures 7(*a*) and 7(*b*) show a typical test object and the radial profile of intensity (along the dashed line), respectively. A parabolic intensity profile was chosen for the test image, to match the observed profiles of the bubble fronts. The corresponding autocorrelation function $\eta(x, y)$ and its azimuthal average $\langle \eta \rangle_\theta$ are shown in figures 8(*a*) and 8(*b*), respectively. The threshold value of 0.3 accurately

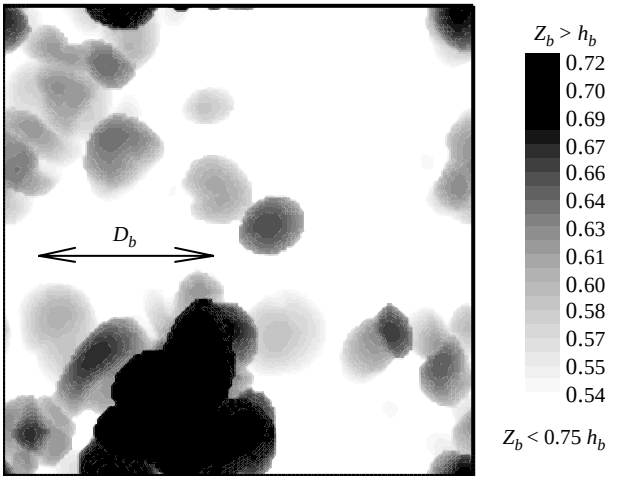

FIGURE 9. Bubble front image $Z_b(x, y)$ from simulation 18 at $Agt^2 = 22$. D_b denotes the mean radius obtained from the autocorrelation procedure.

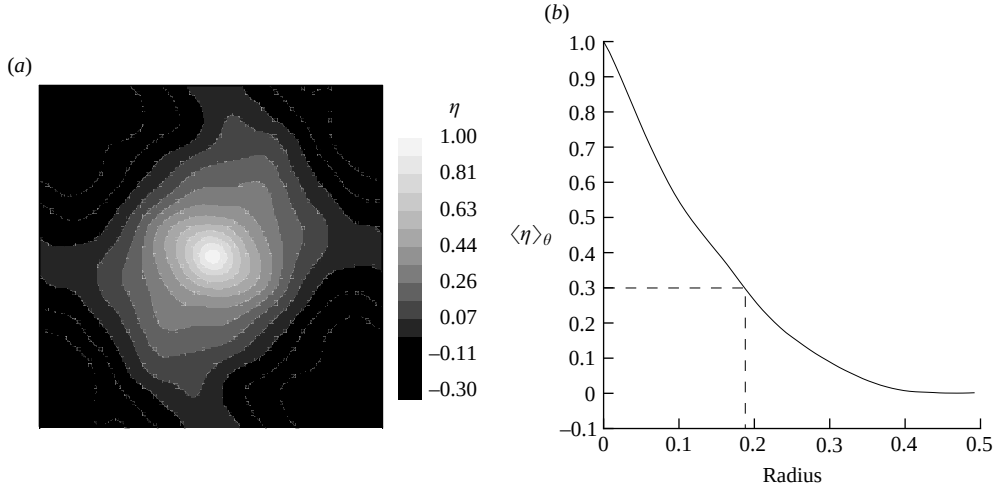

FIGURE 10. (*a*) Autocorrelation contours of the bubblefront field from simulation 18 and the azimuthally averaged radial profile (*b*).

captures the radius of the test object (~ 20 pixels). This procedure was repeated with test objects of different diameters and with multiple objects in a single frame. The error using this technique for these cases was determined to be $\sim \pm 15\,\%$. The robustness of this technique was confirmed by including multiple objects in a single frame, and with different intensity profiles. A sample image of the bubblefront from the mode-coupling case 18 at $Agt^2 = 22$, is shown in figure 9. The results of the autocorrelation technique applied to this image are plotted in figures 10(*a*) and 10(*b*) as the $\eta(x, y)$ contours and the radial profile of $\langle\eta\rangle_\theta$, respectively. Applying the 0.3 cutoff, we determine the average bubble diameter D_b for this image to be ~ 0.38 cm.

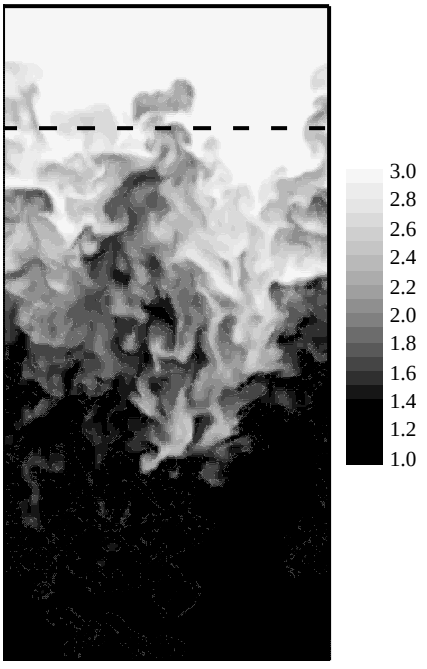

FIGURE 11. Vertical slice of density contours from simulation 10 at $Agt^2 = 17$. The average bubble density and velocities are computed within the volume enclosed by the leading bubble tip and the dashed line.

The Froude number, Fr_0, defined based on the bubble diameter and the associated bubble velocity v_b is

$$Fr_0 = \frac{v_b}{\sqrt{\dfrac{\rho_2 - \rho_1}{\rho_2}\dfrac{gD_2}{2}}}. \tag{26}$$

This definition does not take into account the dilution of bubbles through the entrainment of heavy fluid and subsequent physical (and numerical) diffusion. This process increases the effective density of the bubbles, and it should be accounted for in calculating the Froude number (see Dimonte *et al.* 2004). The effect of entrainment is evident in the vertical slice of density contours from simulation 10 at $Agt^2 = 17$ (figure 11), which shows the leading bubbles as grey rather than black. The effective bubble density ρ_b may then be obtained by averaging the density within a volume defined as the region bounded by max $(Z_b(x, y))$ and the dominant bubble radius $D_b/2$ (in figure 11, this is approximately the region between the leading bubble tip and the dashed line). The bubble velocity is similarly obtained by volume-averaging the vertical velocities in this region, which takes into account the velocity of heavier fluid trapped within and co-moving with the bubble. The Froude-number definition from (26) should then be modified as

$$Fr_{eff} = \frac{v_b}{\sqrt{\dfrac{\rho_2 - \rho_b}{\rho_2}\dfrac{gD_b}{2}}}, \tag{27}$$

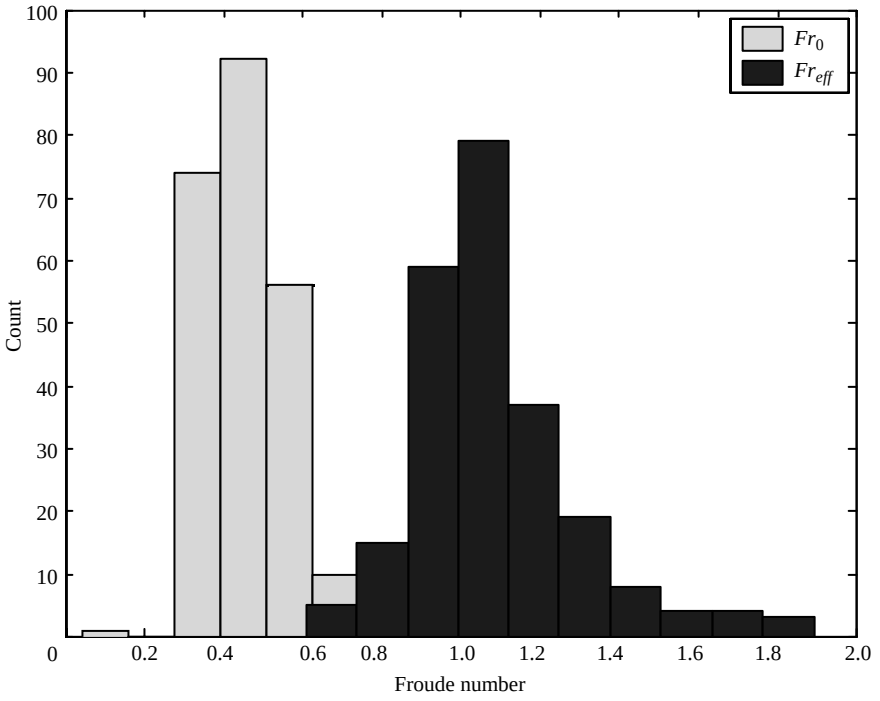

FIGURE 12. Histogram of Froude numbers from the 18 simulations.

where $\rho_1 < \rho_b < \rho_2$. For the density field shown in figure 11, $\rho_b = 2.69\,\mathrm{g\,cm^{-3}}$, $v_b = 0.049\,\mathrm{cm\,s^{-1}}$, $Fr_0 = 0.29$ and $Fr_{eff} = 0.79$. The values of Fr_0 and Fr_{eff} from all the simulations were 0.43 ± 0.12 and 1.04 ± 0.26, respectively. We use the effective Froude number Fr_{eff} in the verification of (6) and (7). Figure 12 shows a histogram of Froude numbers from all the simulations obtained from (26) and (27). Scorer (1957) accounted for entrainment in buoyant thermals and obtained 1.2, which is in reasonable agreement with the values of the effective Froude number reported here. Dimonte & Schneider (2000) report ~ 0.9 from their linear electric motor (LEM) experiments, while Glimm & Li (1988), in their analysis of the rocket rig experiments of Read (1984), obtain a value of 1.1. However, these experimental values were obtained without considering entrainment and numerical diffusion. Davies & Taylor (1950) experimentally obtained $Fr \sim 0.66$ for a lenticular bubble in an open bath.

For $A = 1$, a periodic array of RT bubbles has been shown to have a Froude number of ~ 0.56 from potential flow analysis by Layzer (1955). Gonchorov (2002) and Alon *et al.* (1995) extend Layzer's analysis to $A < 1$, and they determine the bubble velocity as a function of A:

$$v_b = 0.58\sqrt{\frac{2A}{1+A} g \frac{\lambda_b}{2}}. \tag{28}$$

This is equivalent to (26), if we take $D_b \sim \lambda_b$, and $Fr \sim 0.58$. Sohn (2003) alternatively obtained from his potential flow model,

$$v_b = C\sqrt{\frac{Ag\lambda_b}{2}}, \tag{29}$$

which is consistent with (26) if we use Daly's parameterization (Daly 1967) to relate bubble wavelength to diameter

$$\lambda_b = D_b \frac{\rho_1 + \rho_2}{\rho_2}. \tag{30}$$

Equation (30) accounts for the different behaviours of bubbles and spikes at different Atwood numbers. For large A, the spikes are narrow and in free fall, giving $D_b \gg D_s$, and $\lambda_b \sim D_b$. RT flows are symmetric at low Atwood numbers, and (30) accordingly gives $D_b \sim D_s$ and $\lambda_b \sim 2D_b$. However, an analysis of several three-dimensional numerical simulations (Dimonte 2004) shows better agreement with the scaling suggested by (28). Pending further investigation of the dependence of bubble wavelength λ_b on diameter D_b at different A, we use C defined according to (9) to accommodate ambiguities in the bubble wavelength–diameter relation.

Experimental values of Fr for a chaotic bubblefront are believed to be higher than the value obtained from the potential flow models, because RT bubbles probably behave like isolated thermals in an infinite bath rather than structures in a tightly bound periodic lattice. This is because a bubble in an initially periodic lattice that is locally perturbed forward would shoot past its neighbours owing to the reduced counterflow drag experienced by it (from continuity, the spike flow velocity surrounding the bubble would be reduced owing to the increased area). Such an isolated leading bubble could grow self-similarly, with $D_b \sim h_b$. Thus, RT bubbles more likely resemble the buoyant thermals in Scorer's experiment. Glimm *et al.* (1990) invoke an envelope instability of the chaotic bubblefront to explain the observed higher Fr numbers. In their model, the bubble velocity is given by the superposition of the bubblefront velocity and a velocity proportional to the modulation wavelength. We believe that numerical simulations of isolated bubbles can resolve these issues.

Entrainment and fine-scale mixing (triggered by numerical diffusion in MILES) may also lead to a reduction in the numerically obtained values of α_b. For instance, we can account for numerical diffusion by using the effective Froude number in $v_b = Fr_{eff}\sqrt{(\delta\rho/\rho_2)(gD_b/2)}$, where $\delta\rho = \rho_2 - \rho_1$, and combining with (4) to give

$$\alpha_b = \frac{Fr_{eff}^2}{8} \frac{D_b}{h_b} \frac{\rho_1 + \rho_2}{\rho_2}. \tag{31}$$

When bubble densification due to entrainment is considered, (31) produces higher values of $\alpha_b \sim 0.07$, which is in better agreement with experimental values. Simulations that actively track the interface thus suppressing numerical diffusion (front tracking schemes; see Glimm *et al.* 2001; George *et al.* 2002) indeed produce such higher values for α_b $(0.05 - 0.08)$. At late time, however, these simulations also report a reduction in the value of α_b because bubbles entrain and trap heavier fluid within them thus reducing their effective buoyancy. In this paper, we suggest an alternative explanation for the discrepancies in the value of α_b from experiments and numerical simulations – the absence of long wavelengths in simulations.

5.2. *Effect of initial amplitudes*

5.2.1. *Large-scale effects*

Cases 1 to 13 constitute a study of the effect of initial amplitudes on self-similar parameters α_b and β_b. All these cases had an initial spectrum $h_k \sim k^{-2}$, while the minimum imposed modes ranged from $N_{min} = 1$ in some cases to $N_{min} = 3$ in others. To isolate the effect of initial amplitudes, figure 13(a) shows the evolution of bubble amplitudes for cases 1, 3 and 6, all of which had the same values of $N_{min} = 1$.

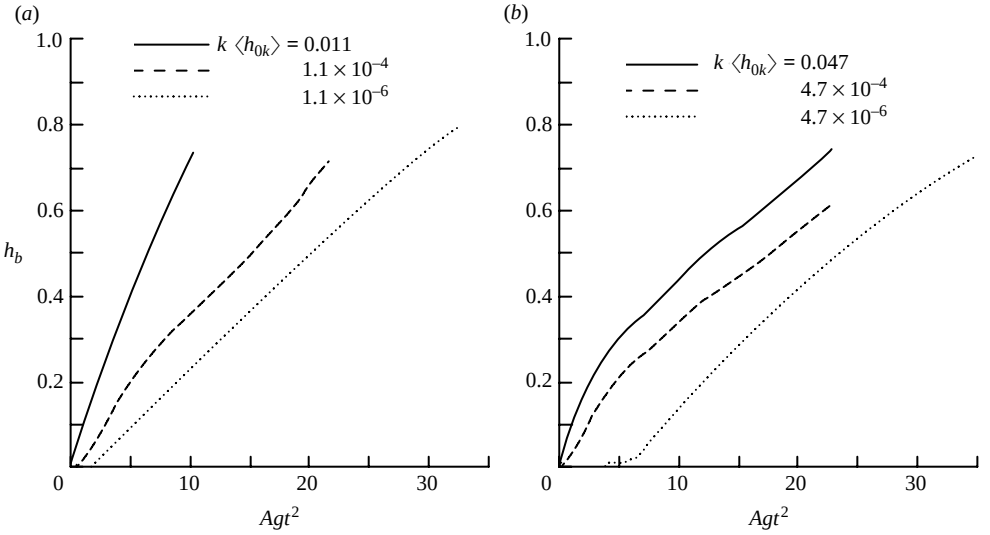

FIGURE 13. Effect of $k\langle h_{k0}\rangle$: (*a*) Evolution of bubble amplitude, h_b for cases 1, 3 and 6 ($N_{min}=1$; $k\langle h_{k0}\rangle = 1.1\times10^{-6}$, 1.1×10^{-4} and 0.011). (*b*) Evolution of bubble amplitude, h_b for mode-coupling cases 16, 17 and 18 ($k\langle h_{k0}\rangle = 4.7\times10^{-6}$, 4.7×10^{-4} and 0.047).

Simulation	α_b	β_b	Effective *Fr* number	Θ	*K.E.*/Δ*P.E.*
1	0.025	0.53 ± 0.08	0.91 ± 0.24	0.76 ± 0.07	0.37 ± 0.07
2	0.024	0.44 ± 0.09	1.14 ± 0.13	0.81 ± 0.07	0.37 ± 0.07
3	0.032	0.41 ± 0.12	1.16 ± 0.19	0.79 ± 0.06	0.38 ± 0.09
4	0.046	0.51 ± 0.06	1.16 ± 0.14	0.73 ± 0.09	0.45 ± 0.07
5	0.048	0.62 ± 0.28	0.91 ± 0.18	0.68 ± 0.07	0.60 ± 0.06
6	0.084	0.73 ± 0.08	1.04 ± 0.20	0.63 ± 0.07	0.58 ± 0.06
7	0.087	0.57 ± 0.1	1.01 ± 0.08	0.68 ± 0.07	0.72 ± 0.07
8	0.021	0.53 ± 0.1	1.05 ± 0.20	0.78 ± 0.05	0.37 ± 0.09
9	0.035	0.45 ± 0.06	1.16 ± 0.17	0.80 ± 0.06	0.46 ± 0.08
10	0.045	0.53 ± 0.12	1.02 ± 0.13	0.75 ± 0.09	0.47 ± 0.09
11	0.028	0.40 ± 0.12	1.47 ± 0.41	0.81 ± 0.05	0.37 ± 0.03
12	0.057	0.64 ± 0.09	0.94 ± 0.18	0.72 ± 0.12	0.50 ± 0.13
13	0.083	0.54 ± 0.09	1.07 ± 0.09	0.70 ± 0.09	0.54 ± 0.15
14	0.037	0.45 ± 0.03	1.12 ± 0.09	0.82 ± 0.1	0.36 ± 0.04
15	0.036	0.43 ± 0.05	1.09 ± 0.12	0.75 ± 0.09	0.38 ± 0.04
16	0.023	0.51 ± 0.10	1.08 ± 0.17	0.72 ± 0.09	0.43 ± 0.15
17	0.026	0.44 ± 0.05	0.94 ± 0.11	0.81 ± 0.06	0.36 ± 0.04
18	0.028	0.47 ± 0.09	1.13 ± 0.18	0.82 ± 0.03	0.38 ± 0.05

TABLE 3. Summary of results from the simulations.

Simulation 6 with $k\langle h_{0k}\rangle = 0.011$ grew the fastest, while the bubble amplitude from simulation 1 with $k\langle h_{0k}\rangle = 1.1\times10^{-6}$ took up to $Agt^2\sim30$ cm to reach 0.75 cm. It is clear from the slope of these curves that the self-similar growth for these simulations is affected by the initial amplitudes. The growth parameter α_b was determined as the derivative of h_b with respect to Agt^2 over the time window $t_k\leqslant t\leqslant t_{mc}$, and is listed for all the cases in table 3. Simulations 16, 17 and 18 were designed to test the effect of the initial amplitudes on α_b and β_b in the mode-coupling limit. All three calculations

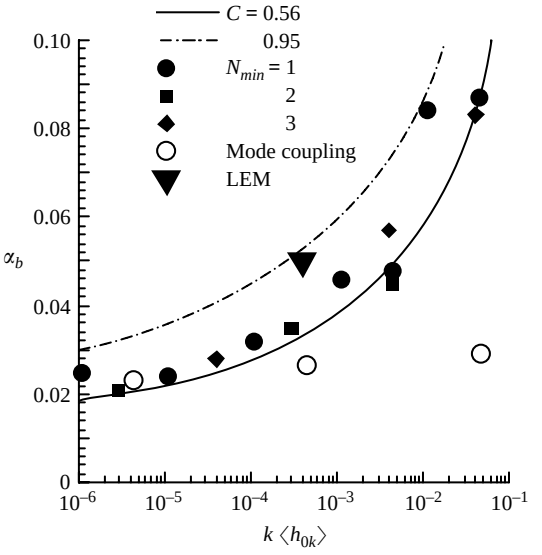

FIGURE 14. Comparison of α_b from the model and NS. Open circles show insensitivity of the mode-coupling cases to the initial amplitudes.

had energy confined to modes 16–32. The values of $k\langle h_{0k}\rangle$ were 4.7×10^{-6}, 4.7×10^{-4} and 0.047 for cases 16, 17 and 18, respectively (note that for these cases, $k\langle h_{0k}\rangle$ is not constant since a k^{-2} spectrum was not used; the value reported here was computed for $k_p = 2\pi/\lambda_p$). Figure 13(*b*) shows the time traces of bubble amplitude for the mode-coupling simulations. Although all three cases saturate at different times owing to different initial amplitudes, they appear to have the same slope during their self-similar evolution. Inspection of table 3, shows that α_b is insensitive to $k\langle h_{0k}\rangle$ when the large scales are generated purely by mode coupling. Furthermore, α_b takes up a lower-bound and universal value of 0.02–0.03 for the mode-coupling simulations (within the error bounds reported here).

These results are summarized in figure 14 by plotting α_b *vs.* $k\langle h_{0k}\rangle$ for all of the simulations in the initial amplitude study. The closed symbols represent cases 1–13, where long wavelengths were present in the initial spectrum and show good agreement with the model, while the open circles refer to the mode-coupling calculations. The data lie between the lines for Dimonte's model with $C = 0.56$ and 0.95. The value of $C < 0.95$ implied by figure 14 could be the result of numerical diffusion, which causes the densification of bubbles and reduces their growth rate. We discuss below a correction to α_b that accounts for numerical diffusion, giving as a result higher values for C. The growth rate obtained from the LEM experiment (Dimonte & Schneider 1996, 2000) at an estimated amplitude of $k\langle h_{0k}\rangle = 4\ 10^{-4}$ is also shown in figure 14. This datapoint falls on the $C = 0.95$ line, possibly because the experiments used immiscible fluids and had less diffusion than the simulations reported here.

The bubble wavelengths λ_b, calculated from D_b using (30), are shown in figure 15(*a*) as a function of the parameter Agt^2. It is clear that even at late times, λ_b does not exceed 0.5 ($N_{min} = 2$), which is the threshold for the onset of mode coupling for these cases. The self-similar parameter $\beta_b = \lambda_b / h_b$ is plotted in figure 15(*b*) and shows a near-constant value of ~ 0.4 for $t > t_k$. Indeed, β_b appears less sensitive to the initial amplitudes than α_b. The linear growth of λ_b and the constancy of β_b shows that

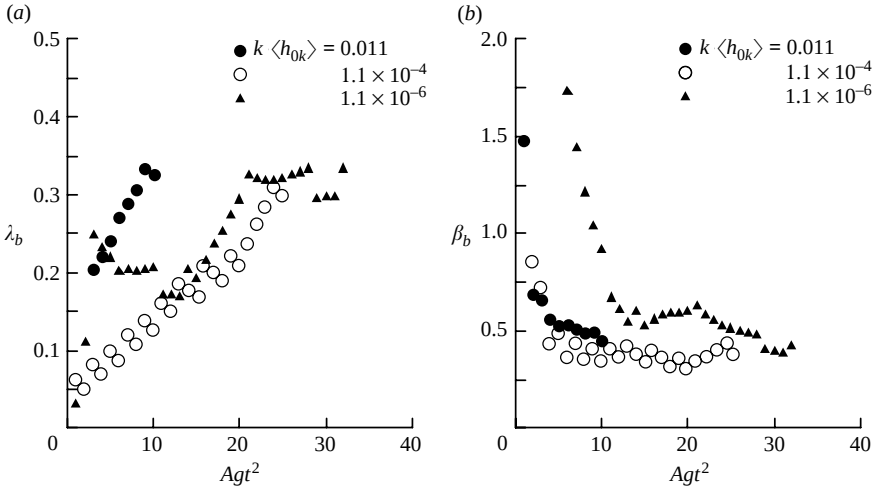

FIGURE 15. Effect of $k\langle h_{k0}\rangle$: (*a*) Evolution of bubble wavelength, λ_b for cases 1, 3, and 6 ($N_{min} = 1$; $k\langle h_{k0}\rangle = 1.1 \times 10^{-6}$, 1.1×10^{-4}, and 0.011) scaled to λ_p. (*b*) Evolution of β_b for cases 1, 3, and 6.

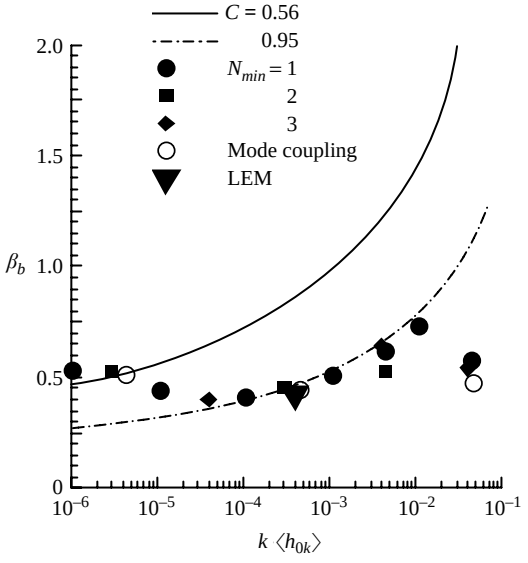

FIGURE 16. Comparison of β_b from the model and Navier–Stokes. Open circles show insensitivity of the mode-coupling cases to the initial amplitudes.

these calculations have reached and maintain self-similarity. The mean β_b for all the simulations were obtained by averaging for $t_k < t < t_{mc}$ and are given in table 3.

Figure 16 shows β_b as a function of $k\langle h_{0k}\rangle$ for the 13 cases that constitute the initial amplitude study and the three mode-coupling cases. (The diameter to amplitude ratio D_b/h_b can be obtained from figure 16 by multiplying by $(1+A)/2$, giving an average value of 0.3. Analysis of laser induced fluorescence images of LEM experiments yield a value of ~ 0.38, Dimonte & Schneider 2000). The simulation points in figure 16 show that β_b is weakly sensitive to $k\langle h_{0k}\rangle$ compared to the model. In general, the β_b values appear to agree with the $C = 0.95$ line (and the LEM datapoint) except at very

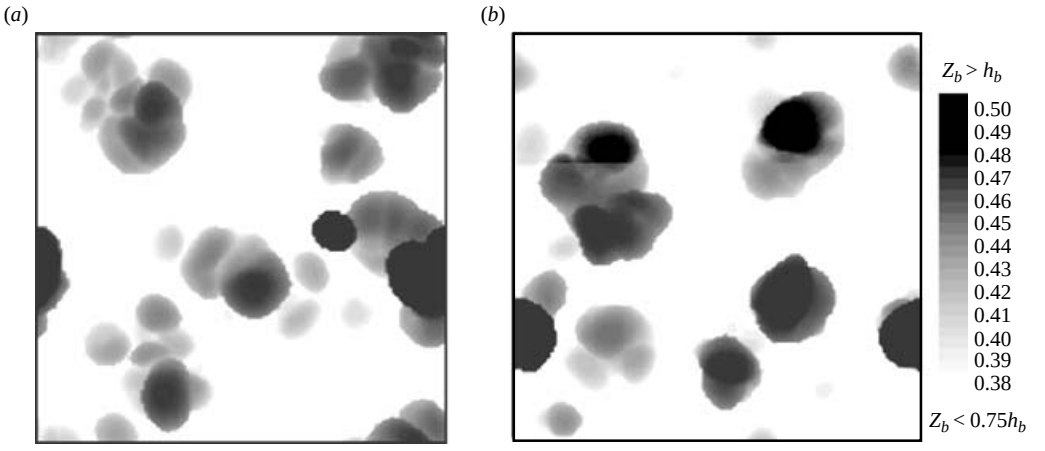

FIGURE 17. Bubblefront images from simulations 1(a) and 6(b). These simulations had $k\langle h_{0k}\rangle = 1.1 \times 10^{-6}$ and 0.011, respectively. The bubblefronts are realized at times when both simulations had the same bubble amplitude h_b.

low and very high amplitudes. The disagreement at high $k\langle h_{0k}\rangle$ ($\geqslant 0.01$) could be due to the initial perturbations approaching their nonlinear saturation limit. Note that α_b also saturates for $k\langle h_{0k}\rangle \geqslant 0.01$, in contrast with the model.

One reason for the reduced sensitivity of β_b at low amplitudes may be mode-coupling effects. Although these calculations were initialized with k^{-2} spectra, mode-coupling may also be present and contribute to the dynamics at late time. Haan (1991) and Dimonte (2004) suggest adding the mode-coupling contributions in quadrature to the long-wavelength amplitudes already present in the initial conditions (ambient modes). If the amplitudes of the ambient modes are low, the relative significance of the mode-coupling products increases. Consequently, α_b and β_b may become less sensitive to $k\langle h_{0k}\rangle$ at small amplitudes. This is seen in the β_b behaviour and, to a smaller extent, in figure 14 for α_b. There appears to be a transition point at $k\langle h_{0k}\rangle \sim 3 \times 10^{-4}$, below which mode-coupling desensitizes β_b. A similar transition occurs at $k\langle h_{0k}\rangle \sim 3 \times 10^{-4}$ for the molecular mix fraction, bubble density and the kinetic energy dissipation (§ 5.2). Furthermore, it is possible that mode-coupling has a greater effect on β_b than on α_b. For instance, the merger of two bubbles of nearly equal diameter would increase β_b by $2^{1/3}$, but the corresponding terminal velocity would be higher by only $2^{1/6}$. Of course, in addition to the terminal velocity, α_b also depends on the length of time Δt over which the merger takes place, i.e. the merger rate. (Cheng, Glimm & Sharp (2002) from their analysis of images from the rocket rig experiment, report the distribution of bubble diameters and their positions, and infer a bubble merger rate from applying single-mode dynamics to the bubble envelope.) Three-dimensional simulations initialized with two different wavelengths may clarify the bubble merger process in detail. Note that in the experiments, both mode-coupling and long-wavelength saturation are present simultaneously, and further studies quantifying the relative importance of each are required to resolve these issues.

Finally, to ensure that the β_b behaviour observed here is not an artefact of the autocorrelation procedure used, we show in figures 17(a) and 17(b) two realizations of the bubblefronts from simulations 1 and 6. The bubblefronts were realized at times such that the simulations had the same bubble amplitude of $h_b \sim 0.5$ cm. For simulation 1 ($k\langle h_{0k}\rangle = 1.1 \times 10^{-6}$) this was at $Agt^2 \sim 20$, while for simulation 6

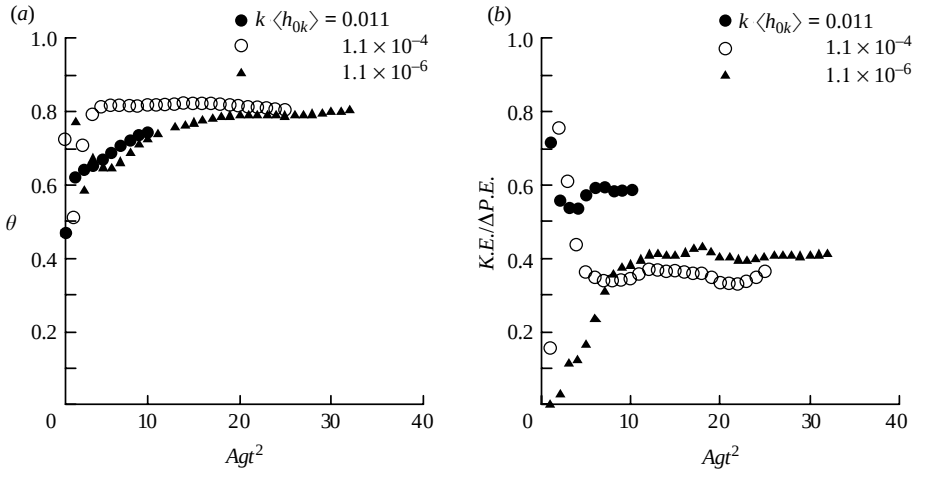

FIGURE 18. Effect of $k\langle h_{k0}\rangle$: (*a*) Evolution of global molecular mix fraction Θ for cases 1, 3 and 6 ($N_{min}=1$; $k\langle h_{k0}\rangle = 1.1\times10^{6}$, 1.1×10^{-4} and 0.011). (*b*) Evolution of $K.E./\Delta$P.E. for cases 1, 3 and 6.

($k\langle h_{0k}\rangle = 0.011$) the bubblefronts were extracted at $Agt^2 \sim 6$. From a visual inspection of figure 17, both images show leading bubbles of roughly the same diameter (and hence the same β_b since the amplitudes are the same) consistent with the results of the autocorrelation analysis. We conclude that while it is possible that β_b is truly insensitive to $k\langle h_{0k}\rangle$ in disagreement with the model, the sensitivity of this parameter may also be muted owing to other factors such as mode-coupling.

5.2.2. *Small scale-effects*

In addition to large-scale effects incorporated in α_b and β_b, small-scale effects such as the global molecular mix parameter Θ were also investigated. Values for Θ were computed from volume fraction profiles as

$$\Theta = \frac{\int \langle f_1 f_2\rangle \mathrm{d}z}{\int \langle f_1 f_2\rangle \mathrm{d}z} \tag{32}$$

where $\langle\bullet\rangle$ once again denotes averaging over the (x, y)-plane. Θ approaches 1 for completely mixed fluids, and 0 for immiscible fluids (Dankwerts 1952). Thus, Θ characterizes the extent of molecular mixing. The evolution of Θ with Agt^2 is shown in figure 18(*a*) for cases 1, 3 and 6. For all these cases, Θ asymptotes to ~ 0.8 consistent with experiments (Wilson & Andrews 2002; Ramaprabhu & Andrews 2004), although at slightly different rates. The simulations and experiments of Dalziel *et al.* (1999) also report a Θ value that asymptotically approaches 0.8. Thus, even with a higher level of diffusion, MILES produces the same level of molecular mixing as the experiments and high-resolution DNS. The high-resolution MILES study of Youngs (2003) gives a value of 0.81 for Θ in the self-similar stage. The nonlinear coupling of wavelengths can yield both low- and high-wavenumber products. If the daughter products have wavelengths smaller than the zone size employed in these simulations, this leads to the augmentation of the numerical viscosity and greater molecular mixing. Furthermore, Θ appears weakly sensitive to $k\langle h_{0k}\rangle$ (figure 19). The large-amplitude cases (with

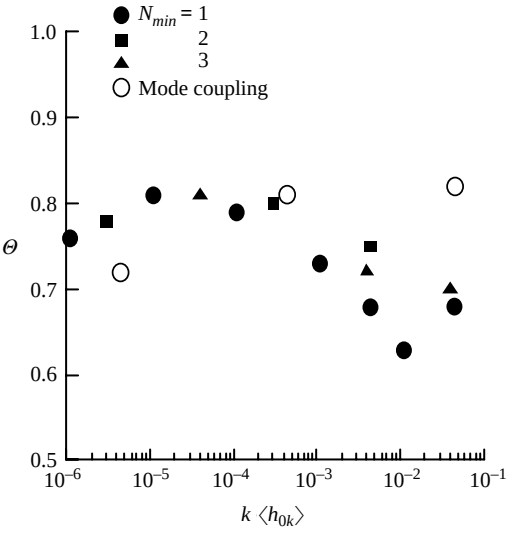

FIGURE 19. Global molecular mix fraction Θ *vs.* $k\langle h_{k0}\rangle$.

$N_{min} = 1$) register a slightly lower value, approaching 0.6. This could be due to large-scale vortical motion that transports unmixed lighter fluid into regions of heavier fluid and vice versa (i.e. entrainment without molecular mixing). The simulations by Youngs (2003) in which long wavelengths were included also exhibit reduced molecular mixing ($\Theta \sim 0.68 - 0.74$).

Ramaprabhu & Andrews (2004) suggest that in the presence of molecular mixing, α_b is modified as,

$$\tilde{\alpha} = \alpha\sqrt{1-\Theta}. \tag{33}$$

For $\Theta \sim 0.8$, (33) implies a halving of the growth rate owing to molecular mixing. This could reconcile the values of α_b obtained from MILES and front-tracking simulations, which actively suppress molecular mixing (front-tracking simulations give $\alpha_b \sim 0.07$, while LES and DNS give $\sim 0.02 - 0.03$ for the mode-coupling cases). George *et al.* (2002) apply a correction to the Atwood number to account for numerical diffusion, raising their α-value from 0.035 to 0.06 in their TVD simulations. Also, if a correction such as (33) is applied, the α_b values in figure 14 would suggest higher values for *Fr* closer to experimental values. The reduction of α_b suggested by (33) is an upper bound, because Θ is a global parameter defined for both bubbles and spikes. If we consider (33) for leading bubbles, $\tilde{\alpha} \approx 0.7\alpha$ for miscible experiments.

The self-similar evolution of RT instabilities involves the conversion of initially available potential energy (*P.E.*) to kinetic energy (*K.E*) as the flow develops. The ratio of the kinetic energy of the flow to the accompanying loss in potential energy is nearly constant for such flows (Youngs 1994). We use the approach outlined in Dimonte *et al.* (2004) to define this ratio: assuming for low A, a linear profile of the volume fractions, and $h_s \sim h_b = h$, the loss in potential energy may be written as

$$\Delta P.E. = \int_{-h}^{0} (\rho_1 - \langle\rho\rangle) g z \,\mathrm{d}z + \int_{0}^{h} (\langle\rho\rangle - \rho_1) g z \,\mathrm{d}z \approx \frac{(\rho_2 - \rho_1) g h^2}{6}. \tag{34}$$

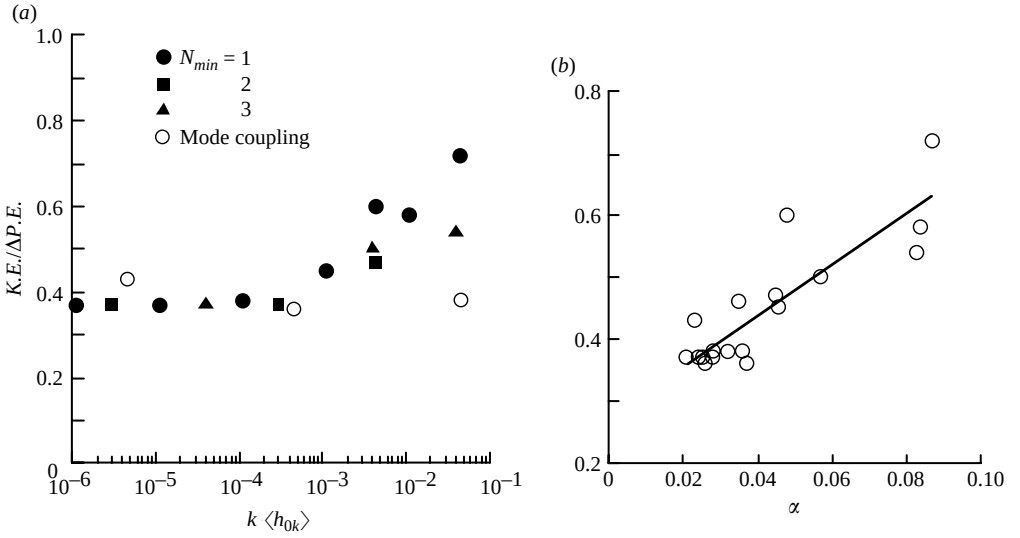

FIGURE 20. (*a*) Kinetic energy as a fraction of potential energy released *vs.* $k\langle h_{0k}\rangle$. (*b*) Correlation between *K.E.*/Δ*P.E.* and α_b. The solid line represents *K.E.*/Δ*P.E.* $= 11.9\alpha_b$.

In the above, the error in assuming $h_s \sim h_b$ results in an overall error in Δ*P.E.* of $\pm 5\,\%$ for these calculations. The corresponding gain in kinetic energy is then,

$$K.E. = \tfrac{1}{2}\int \rho(\boldsymbol{v}\cdot\boldsymbol{v})\,\mathrm{d}x\,\mathrm{d}y\,\mathrm{d}z, \tag{35}$$

where the integral is performed over the entire computational domain. The ratio *K.E.*/Δ*P.E.* is plotted for cases 1, 3 and 6 in figure 18(*b*). The fraction of energy dissipated is given by $1 - K.E./\Delta P.E.$, and approaches a value slightly greater than 50 % for these simulations. This is in good agreement with the experiments of Ramaprabhu & Andrews (2004), who report a value of $D/\Delta P.E. = 49\,\%$ from their simultaneous measurements of density and velocity fields. Figure 20(*a*) is a plot of *K.E.*/Δ*P.E.* from all the simulations, and shows a slight increase with $k\langle h_{0k}\rangle$. Dimonte *et al.* (2004) argue that the ratio *K.E.*/Δ*P.E.* bears a strong correlation with α_b for the leading bubbles. In the limit of small density differences, they obtain

$$K.E./\Delta P.E. \sim 20\alpha_b. \tag{36}$$

K.E./Δ*P.E.* from the current simulations are plotted as a function of α_b in figure 20(*b*), giving *K.E.*/Δ*P.E.* $\sim 12\alpha_b$, slightly different from (36) probably due to the finite Atwood number employed in this work. The bubble density ρ_b, defined earlier in this section, is shown as a function of $k\langle h_{0k}\rangle$ in figure 21. The molecular mix fraction, kinetic energy dissipation, and the bubble density all undergo a transition at $k\langle h_{0k}\rangle \sim 3\times 10^{-4}$, below which they remain nearly constant, while varying with $k\langle h_{0k}\rangle$ at higher amplitudes.

The ratio of the horizontal to the vertical components of kinetic energies,

$$X = \frac{(K.E._{.x} + K.E._{.y})}{K.E._{.z}} \tag{37}$$

from these simulations was determined to be ~ 0.64. In comparison, the LES of Youngs (1994) gives a value of ~ 0.48 for *K.E.*/Δ*P.E.* and ~ 0.7 for the ratio of kinetic energy components. These values are slightly lower than the experimentally

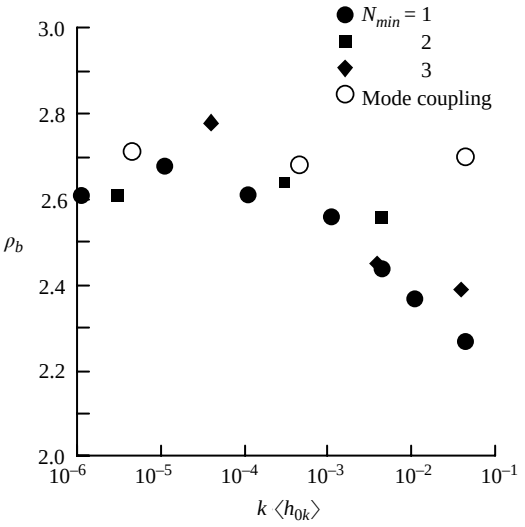

FIGURE 21. Variation of bubble density ρ_b with $k\langle h_{k0}\rangle$.

observed values of 0.78 for X inferred from a velocity ratio of ~ 1.6 obtained from particle image velocimetry measurements (Ramaprabhu & Andrews 2004). The values of mixing parameter Θ and $K.E./\Delta P.E.$ are summarized in table 3. Simulation 6, which is the most efficient in extracting kinetic energy from the initial density distribution ($K.E./\Delta P.E. \sim 0.6$), also has the lowest value for the mixing parameter Θ. This simulation had $N_{min} = 1$, and the highest growth rate ($\alpha_b \sim 0.08$), which implies the appearance of large-scale structures at early times. Thus, the rate of extraction of potential energy was much higher for this case. A detailed discussion of the effect of the minimum mode is deferred until § 5.4. In summary, while α_b appears sensitive to initial conditions, β_b, the molecular mixing parameter Θ, and $K.E./\Delta P.E.$ all seem to have little memory of the initial spectral content. These findings are further supported by density spectra, which are presented later in this section.

5.3. *Effect of spectral index*

Cases 10, 14 and 15 had the same $k\langle h_{0k}\rangle = 0.0044$ and $N_{min} = 2$, but spectral indices of $p = -2, 0$ (white noise) and -1, respectively. For $p = -1$ and $p = 0$, $k\langle h_{0k}\rangle$ varies with k (from the definition of $\langle h_{0k}\rangle$) and a value based on the dominant wavenumber $k_p = 2\pi/\lambda_p$ was used. From the time traces of h_b, it was observed that the $p = 0$ case grew the fastest initially because the high-wavenumbers of the flat white noise spectrum have a higher energy. However, the growth is slowed down at late times, when the low-amplitude low wavenumbers of this spectrum were sampled by the flow. The corresponding bubble parameters α_b and β_b are plotted in figures 22(a) and 22(b), respectively, and show little sensitivity to p.

5.4. *Effect of longest wavelength imposed*

Cook & Dimotakis (2001) obtained different growth rates for simulations initialized with different peak wavenumbers. They used spectra with peaks centred at mode numbers of 4, 9 and 12, and found that α_b decreased slightly with increasing N_{min}. However, these cases probably evolved through mode-coupling, thus reducing the sensitivity of α_b to N_{min}. In addition, for their cases initialized with $N_{min} = 4$ and $N_{min} = 9$, self-similarity was not achieved. In our study, cases 5, 10 and 12 had spectral

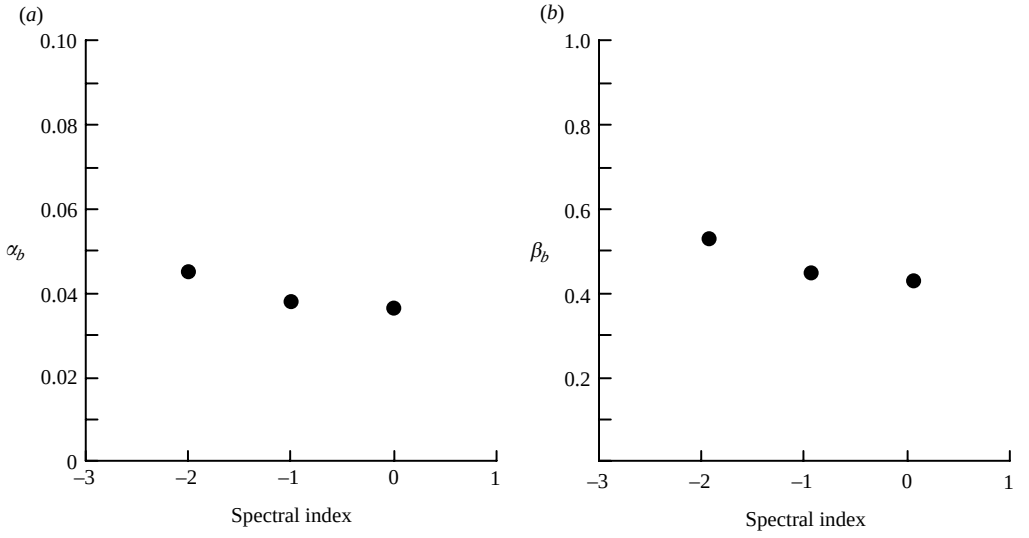

FIGURE 22. Effect of spectral index (SI) on (a) α_b and (b) β_b.

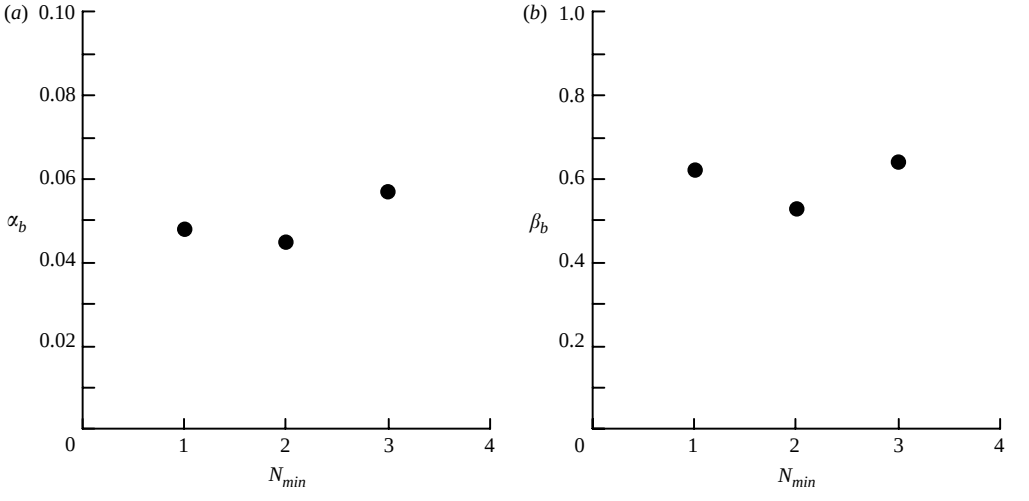

FIGURE 23. Effect of longest wavelength imposed (N_{min}) on (a) α_b and (b) β_b.

peaks at mode numbers 1, 2 and 3, respectively, (thus reducing the mode-coupling contribution), and all had the same amplitude $k\langle h_{0k}\rangle = 0.004$. Figures 23($a$) and 23($b$) are plots of α_b and β_b for various values of N_{min}. Although both parameters vary slightly with the minimum mode number, there appears to be no clear trend. As found previously for the initial amplitude and mode-coupling cases, the global molecular mix fraction Θ and the kinetic energy dissipation showed little dependence on the initial spectral content.

The volume fraction spectra was computed from the (x, y)-distribution of f_1 at $z = 0$ using (Dimonte *et al.* 2004),

$$E_{f_1}(n) = 2\pi n\langle f_1(n)^2\rangle_\theta, \tag{38}$$

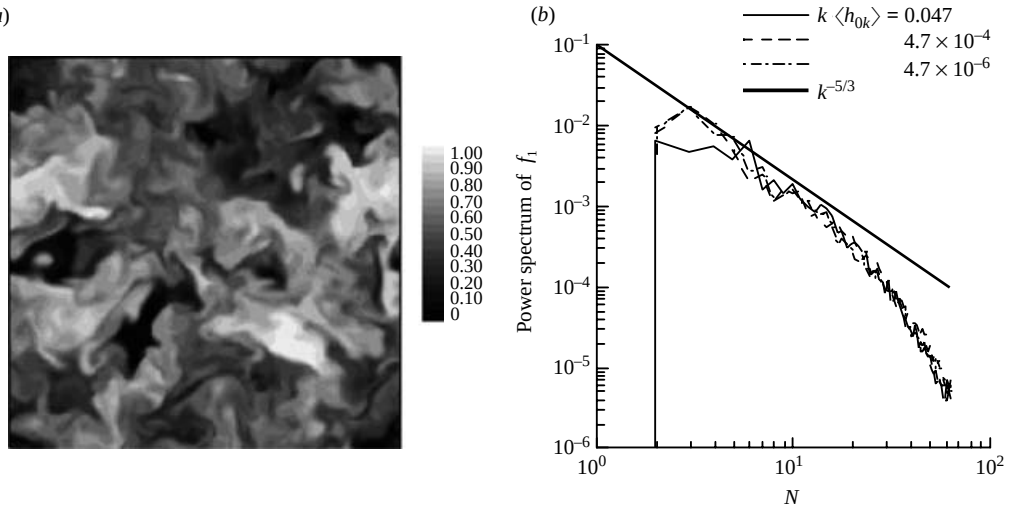

FIGURE 24. (*a*) Contours of volume fraction f_1 on a horizontal plane at $z=0$ (from case 18). (*b*) Azimuthally averaged power spectra of f_1 for the two mode-coupling cases 16, 17 and 18.

where $\langle\bullet\rangle_\theta$ denotes azimuthal averaging. As before, this definition ensures that $\int_0^\infty E_{f_1}(k)\,\mathrm{d}k = \langle f_1^2\rangle - \langle f_1\rangle^2$. Figure 24(*a*) is an image of $f_1(x, y)$ at $z=0$ from simulation 18 at $Agt^2 = 22$, where the large scales are generated purely through mode-coupling. The corresponding azimuthally averaged spectra for the mode-coupling cases 16, 17 and 18 are shown in figure 24(*b*). As described earlier, $\langle\bullet\rangle_\theta$ was obtained by azimuthally averaging over 30 angles. The solid line indicates the $-5/3$ slope and shows the presence of a short inertial range with $k^{-5/3}$. The Reynolds number at $Agt^2 = 22$ may be estimated as

$$Re = \sqrt{\frac{gA_t}{6}}\,\frac{(h_b + h_s)^{3/2}}{\nu} \approx 925, \tag{39}$$

where ν was determined using the procedure described in § 4. Higher resolution simulations at higher Reynolds numbers are expected to give a broader inertial range than observed here. The corresponding Kolmogorov length scale is (Tennekes & Lumley 1972)

$$\eta_k = \frac{h_b + h_s}{2} Re^{-3/4}, \tag{40}$$

and exceeds the Nyquist cutoff associated with the current resolution at $Agt^2 \sim 4$. At higher mode numbers, a dissipative region with a slope of -3 is also evident. Although the mode-coupling cases differed from each other in their initial amplitudes by a factor of 100, their late-time spectra have very similar structures, even in the large-scales, which is consistent with the results of § 5.

The azimuthally averaged power spectra from the initial amplitude study and the spectral index study are shown in figure 25(*a*) and 25(*b*), respectively. Similar to the mode-coupling cases, these spectra have a short inertial range with $E(k) \sim k^{-5/3}$ and a steeper dissipative range. The initial amplitude cases have dissimilar structure at the lowest wavenumbers, which is consistent with the different values of the growth constant obtained from these simulations. At the higher wavenumbers, all of these calculations have nearly identical energies. As we have seen, this similarity is

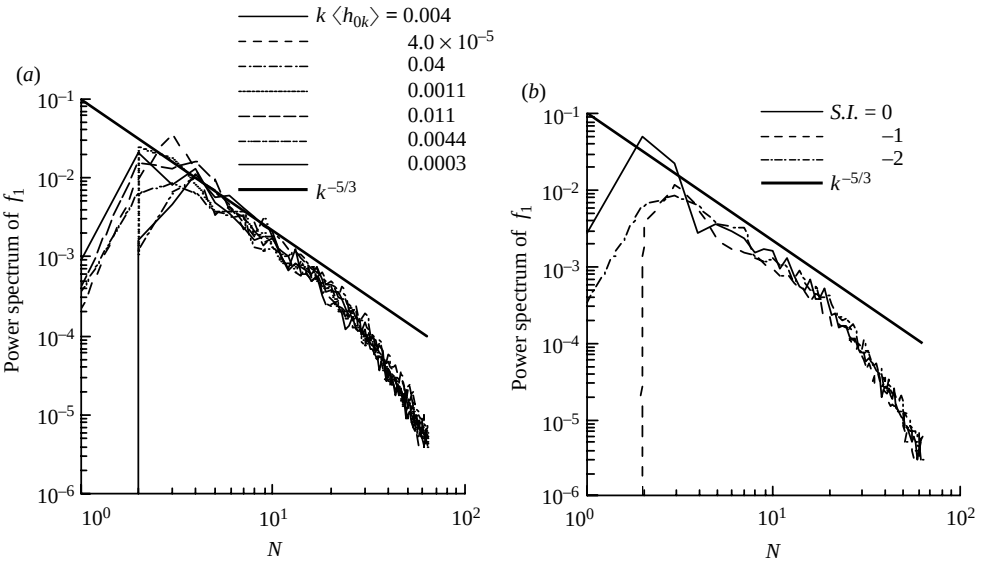

FIGURE 25. Azimuthally averaged power spectra of f_1 from (*a*) the initial amplitude study and (*b*) the spectral index study.

manifested in the small-scale quantities such as the molecular mixing parameter and the kinetic energy dissipation, which show little dependence on the initial conditions. Consistent with the results discussed in § 5.3, the spectral index cases show good collapse both at the large and small scales.

6. Summary and conclusions

Using numerical simulations with carefully specified initial conditions, we have demonstrated that long-wavelength initial amplitudes increase the RT bubble growth parameter α_b to experimentally observed values. There are two limiting scenarios for self-similar growth of RT:

(*a*) Nonlinear coupling of saturated short wavelengths (merger).

(*b*) Amplification and saturation of ambient modes (competition).

Experiments by Dimonte & Schneider (2000) and Ramaprabhu & Andrews (2004) have shown the presence of long wavelengths in their initialperturbations, suggesting that experiments do not evolve purely through merger. We conclude that these two processes exist simultaneously in experiments, and are in competition with each other.

To test these ideas, we performed numerical simulations with and without long wavelength content in the initial conditions. In these simulations, the non-dimensional initial amplitudes ($k\langle h_{0k}\rangle$) varied from $\sim 10^{-6}$ to 10^{-1}. We show that with broadband perturbations, α_b increases logarithmically with the initial amplitudes even after ~ 3.7 generations of bubble evolution (this implies that slight variations in the value of α_b observed in experiments, could in fact be due to large ($100\times$) differences in the initial amplitudes). Conversely, in the pure mode-coupling limit α_b takes up a universal, lower bound value of ~ 0.025. These ideas were formalized by Dimonte (2004), and have been verified through our simulations. The role of initial conditions in the evolution of turbulent RT flow was also studied by Dalziel *et al.* (1999), who reported sensitivity of α_b to the presence of long-wavelength information in their initial conditions.

In an earlier study, the mode-coupling limit was explored in detail by comparing results from different benchmark codes used in RT (Dimonte *et al.* 2004). Many RT simulations are initialized with an annular spectrum (Cook & Dimotakis 2001; Young *et al.* 2001; Youngs 2003), and evolve purely through mode-coupling. We offer this as an explanation for the discrepancies in α_b obtained from simulations and experiments. In this paper, we have shown that with a broadband spectrum, numerical simulations can produce the higher growth rates observed in experiments. We are able to reproduce experimental results even with the numerical diffusion present in our simulations. In fact, front-tracking simulations (Glimm *et al.* 1990) also give lower growth rates at late time (when entrainment and diffusion reduce the local buoyancy driving forces) suggesting that numerical diffusion alone is not sufficient to explain these differences.

Note that mode-coupling exists even in simulations initialized with broadband perturbations. This can be described by adding the daughter products of mode-coupling in quadrature to the amplitudes of the ambient modes. This decreases the sensitivity of α_b and other self-similar parameters at low amplitudes of the ambient perturbations. At higher $k\langle h_{0k}\rangle$, the amplification rate exceeds the mode-coupling rate and α_b and β_b exhibit greater sensitivity to the initial amplitudes. This transition from mode-coupling dominance to a scenario dominated by bubble competition occurs in our simulations at $k\langle h_{0k}\rangle \sim 3 \times 10^{-4}$. While it is unclear how these two effects may be isolated, we suggest simulations of the interactions of three-dimensional bubbles of different wavelengths to study the bubble merger rates, which may be used to quantify the effect of mode-coupling on α_b and β_b.

Both α_b and β_b are reduced in value by the densification of bubbles owing to entrainment and numerical diffusion. Some of this diffusion is due to the inability of the numerical scheme to resolve small scales generated as a result of mode-coupling. Two modes n_1 and n_2 can interact nonlinearly to give products $n_1 - n_2$ and $n_1 + n_2$. If $n_1 + n_2 > 24$, these modes cannot be captured at the current resolution, resulting in numerical diffusion.

While α_b and β_b represent the large-scale dynamics of the flow, small-scale effects such as the molecular mix fraction Θ, the bubble density ρ_b, and the kinetic energy dissipation are weakly sensitive to $k\langle h_{0k}\rangle$. These parameters also transition from mode-coupling to bubble competition at $k\langle h_{0k}\rangle = 3 \times 10^{-4}$, suggesting that this may be a universal transition point. As noted previously, when the bubble behaviour is considered separately, the entrainment and molecular diffusion within the bubbles increase slightly with the initial amplitudes. These observations are supported by centreline density spectra from the simulations, which show variations at the large scales (α_b) and convergence to a uniform structure at the small scales (Θ and $D/\Delta P.E.$). Thus, it appears that the variation of these parameters is due indirectly to large-scale vortical motion (entrainment), and not localized small-scale dynamics (diffusion).

To calculate β_b, the bubble diameter was first computed using an autocorrelation procedure, and then related to the bubble wavelength using Daly's parameterization ($\lambda_b = D_b 2/(1 + A)$). This definition was proposed by Daly (1967) to account for the dissimilar behaviours of bubbles and spikes in different Atwood regimes. At small A, the flow is symmetric and the spikes and bubbles are of the same size and $\lambda_b \sim 2D_b$, whereas at large A, the spikes are very narrow and $\lambda_b \sim D_b$. However, Sohn (2003) and Gonchorov (2002) obtain $\lambda_b \sim D_b$ independent of A, from their potential flow analyses of single-mode RT flows in contrast to Daly. Published numerical simulations (Tryggvason & Unverdi 1990; Li, Jin & Glimm 1996; Dimonte *et al.* 2004) of single-mode RT flows do not conclusively support one scaling over the other. In these

single-mode studies, a periodic array of RT bubbles was considered. We believe that in the self-similar regime, RT bubbles are more likely to resemble isolated thermals in an infinite bath. This is because a localized perturbation to an RT bubblefront with a periodic structure would cause the perturbed bubble to rise up with a velocity proportional to the square root of the perturbation wavelength. The reduced counter-flow drag experienced by such a leading bubble would also contribute to a higher *Fr* number (~ 1) in agreement with experiments and the numerical simulations reported here. Further simulations of such isolated RT bubbles, outside the scope of this work, are required to determine the correct scaling relationship.

To complete the investigation, other effects such as the structure of the initial spectra (characterized by the slope), and the longest wavelength imposed were also considered. Spectra with amplitudes varying as k^{-2}, k^{-1} and k^0, but with the same r.m.s. amplitudes $k\langle h_{0k}\rangle$ were used (to satisfy the condition for self-similarity, a k^{-2} spectral structure is required). To study the effect of the longest wavelength imposed in the initial conditions, the smallest mode-number in the wavepacket, N_{min} was varied from 1 to 3. Both studies show that α_b and β_b (and the small-scale parameters) are insensitive to such effects. For much higher values of N_{min}, we expect mode-coupling to play a more dominant role, accompanied by a decrease in α_b.

Furthermore, α_b can also depend on the extent of physical or numerical diffusion, and other stabilizing mechanisms. For instance, α_b increased by 20 % in the LEM experiments with high surface tension between the fluids (Dimonte & Schneider 2000). Higher-resolution simulations (preferably DNS) and experiments are required to test these issues in greater detail.

P. R. and M. J. A. wish to acknowledge support from the Department of Energy, High Energy Density Science Program under contracts DE-FG03-99DP00276/A000, DE-FG03-02NA00060. The work of G. D. was performed under the auspices of the US Department of Energy by Los Alamos National Laboratory under contract number W-7405-ENG-36. The authors also wish to thank the Texas A&M University Supercomputing facility, for permitting use of their computing resources. Finally, the authors would like to thank the referees for their comments which have improved this paper subsantially, particularly the suggestions of one reviewer which led to the inclusion of figure 20(*b*).

Appendix. Model formulation

A synopsis of the model describing the role of initial conditions on α_b and β_b is provided here (for a detailed description, see Dimonte 2004). The transition to nonlinearity of a mode k of amplitude h_k occurs when $kh_k \sim 1$, as the linear velocity of the mode $\sim \Gamma h_k$, approaches its terminal velocity $\sim \sqrt{A_t g/k}$ – this is referred to as the Fermi transition (Layzer 1955). Haan (1989) considered the interaction of neighboring modes of similar phases that can interfere constructively, triggering transition at smaller initial amplitudes. In this scenario, the modes in a wavepacket of width δk transition when their r.m.s. amplitude defined as

$$\langle h_k\rangle = \left(\frac{L^2}{2\pi}\int_{k-\delta k}^{k+\delta k} h_k^2 k'\,\mathrm{d}k'\right)^{1/2}, \tag{A 1}$$

exceeds the nonlinear threshold (thus, the threshold for nonlinear transition is modified as $k\langle h_k\rangle \sim 1$, where k is now the central wavenumber of the wavepacket). Dimonte (2004) estimates the width of the wavepacket as $\delta k \sim 3k/8$. In this picture, the central

wavenumber is the bubble wavenumber k_b, and the width of the wavepacket is $\delta k = (k_b - k_s)/2$, where k_s is the wavenumber of the mode that has just reached its saturation amplitude. An e^{-2} profile is assumed for the energy distribution of the wavepacket with the peak at k_b.

If we take h_b to be the leading bubble amplitude (i.e. of the central mode), then the variance of amplitudes range from 0 to h_b^2, and the mean of these fluctuations is $\langle h_k \rangle^2 = h_b^2/2$ or $\langle h_k \rangle \sim h_b$ (Haan 1989). Then, applying the Fermi transition ($\Gamma h_b = C\sqrt{A_t g \lambda_b/2}$) to the bubble in a wavepacket, we obtain

$$k_b \langle h_k \rangle \sim C\sqrt{\pi}. \tag{A 2}$$

The evolution of $\langle h_k \rangle$ in the nonlinear regime can be written as

$$h_b = \langle h_k \rangle = C\sqrt{\pi}\left(\frac{1}{k} + Fr\sqrt{\frac{Ag}{k}}(t - t_k)\right), \tag{A 3}$$

where t_k is the time at which the nonlinear saturation occurs. Here, t_k is obtained by inverting $h_k = \cosh(\sqrt{Akgt})$ and using (A 2):

$$t_k \sim \frac{1}{\sqrt{Akg}} \cosh^{-1}\left[\frac{C\sqrt{\pi}}{k\langle h_{0k}\rangle}\right]. \tag{A 4}$$

Thus, the self-similar bubble amplitude has been expressed as a function of the initial r.m.s. amplitude $\langle h_{0k} \rangle$ and a modified Froude number C. The dominant wavelength λ_b in the wavepacket is obtained by finding the maximum of (A 3):

$$\frac{\partial h_b}{\partial \lambda_b} = \frac{C}{2\sqrt{\pi}}\left(\sqrt{\frac{Ag}{2\lambda_b}}t + 1 - \ln\left(\frac{C\sqrt{\pi}}{k_b\langle h_{0k}\rangle}\right)\right) = 0, \tag{A 5}$$

This gives

$$\lambda_b = \frac{\pi A g t^2}{2\left(\ln\left(\dfrac{2C\sqrt{\pi}}{k_b\langle h_{0k}\rangle}\right) - 1\right)^2}. \tag{A 6}$$

Combining (A 6) with (A 3), and the definition for β_b, we get two equations describing the dependence of α_b and β_b on $k\langle h_{0k}\rangle$:

$$\alpha_b = \frac{C\sqrt{\pi}}{4}\left[\ln\left(\frac{2C\sqrt{\pi}}{k_b\langle h_{0k}\rangle}\right) - 1\right]^{-1}, \tag{A 7}$$

$$\beta_b = \frac{2\sqrt{\pi}}{C}\left[\ln\left(\frac{2C\sqrt{\pi}}{k_b\langle h_{0k}\rangle}\right) - 1\right]^{-1}, \tag{A 8}$$

Thus according to this model, both α_b and β_b depend logarithmically on $k\langle h_{0k}\rangle$ (qualitatively similar to Birkhoff's model 1955). For self-similarity (constant α_b and β_b), (A 1), (A 7) and (A 8) require that $h_k \sim k^{-2}$.

REFERENCES

Alon, U., Hecht, J., Ofer, D. & Schvarts, D. 1995 Power laws and similarity of Rayleigh–Taylor and Richtmeyer–Meshkov mixing fronts at all density ratios. *Phys. Rev. Lett.* **74**, 534–537.

Andrews, M. J. 1995 Accurate computation of convective transport in transient two-phase flow. *Intl J. Numer. Meth. Fluids* **21**, 205–222.

Andrews, M. J. & Spalding, D. B. 1990 A simple experiment to investigate two-dimensional mixing by Rayleigh–Taylor instability. *Phys. Fluids* A **2**, 922–927.

Birkhoff, G. 1955 Taylor instability and laminar mixing. *University of California Rep.* LA-1862.

Chandrasekhar, S. 1961 *Hydrodynamic and Hydromagnetic Stability*. Clarendon.

Cheng, B., Glimm, J. & Sharp, D. H. 2002 A three-dimensional renormalization group bubble merger model for Rayleigh–Taylor mixing. *Chaos* **12**, 267–274.

Cherfils, C. & Mikaelian, K. O. 1996 Simple model for the turbulent mixing width at an ablating surface. *Phys. Fluids* **8**, 522–535.

Collins, R. 1967 The effect of a containing cylindrical boundary on the velocity of a large gas bubble in a liquid. *J. Fluid Mech.* **28**, 97–112.

Cook, A. W. & Dimotakis, P. E. 2001 Transition stages of Rayleigh–Taylor instability between miscible fluids. *J. Fluid Mech.* **443**, 69–99 (and corrigendum **457**, 2002, 410–411).

Daly, B. J. 1967 Numerical study of two fluid Rayleigh–Taylor instability. *Phys. Fluids* **10**, 297–307.

Dalziel, S. B. 1993 Rayleigh–Taylor instability: experiments with image analysis. *Dyn. Atmos. Oceans* **20**, 127–153.

Dalziel, S. B., Linden, P. F. & Youngs, D. L. 1999 Self-similarity and internal structure of turbulence induced by Rayleigh–Taylor instability. *J. Fluid Mech.* **399**, 1–48.

Dankwerts, P. V. 1952 The definition and measurement of some characteristics of mixtures. *Appl. Sci. Res.* **3** (A), 279–296.

Davies, R. M. & Taylor, G. I. 1950 The mechanics of large bubbles rising through extended liquids and through liquids in tubes. *Proc. R. Soc. Lond.* A **200**, 375–390.

DeNeef, P. 1975 Two waves on a beam plasma system. *Phys. Fluids* **18**, 1209–1212.

Dimonte, G. 1982 Experimental test of modulational theory and stochasticity of nonlinear oscillations. *Phys. Fluids* **25**, 604–607.

Dimonte, G. 2004 Dependence of turbulent Rayleigh–Taylor (RT) instability on initial perturbations. *Phys. Rev.* E **69**, 056305.

Dimonte, G. & Schneider, M. 1996 Turbulent Rayleigh–Taylor instability experiments with variable acceleration. *Phys. Rev.* E **54**, 3740–3743.

Dimonte, G. & Schneider, M. 2000 Density ratio dependence of Rayleigh–Taylor mixing for sustained and impulsive acceleration histories. *Phys. Fluids* **12**, 304–321.

Dimonte, G., Youngs, D. L., Dimits, A. *et al.* 2004 A comparative study of the turbulent Rayleigh–Taylor (RT) instability using high-resolution 3D numerical simulations: The Alpha-Group collaboration. *Phys. Fluids* **16**, 1668–1692.

George, E., Glimm, J., Li, X-L., Marchese, A. & Xu, Z.-L. 2002 A comparison of experimental, theoretical, and numerical simulation of Rayleigh–Taylor mixing rates. *Proc. Natl Acad. Sci.* **99**, 2587–2592.

Glimm, J., Grove, J. W., Li, X. L., Oh., W. & Sharp, D. H. 2001 A critical analysis of Rayleigh–Taylor growth rates. *J. Comput. Phys.* **169**, 652–677.

Glimm, J. & Li, X. L. 1998 Validation of Sharp–Wheeler bubble merger model from experimental and computational data. *Phys. Fluids* **31**, 2077–2085.

Glimm, J., Li, X. L., Menikoff, R., Sharp, D. H. & Zhang, Q. 1990 A numerical study of bubble interactions in Rayleigh–Taylor instability for compressible fluids. *Phys. Fluids* A **2**, 2046–2054.

Gonchorov, V. N. 2002 Analytical model of nonlinear, single-mode, classical Rayleigh–Taylor instability at arbitrary Atwood numbers. *Phys. Rev. Lett.* **88**, 134502.

Haan, S. W. 1989 Onset of nonlinear saturation for Rayleigh–Taylor growth in the presence of a full-spectrum of modes. *Phys. Rev.* A **39**, 5812–5825.

Haan, S. W. 1991 Weakly nonlinear hydrodynamic instabilities in inertial fusion. *Phys. Fluids* B **3**, 2349–2355.

Inagamov, N. A. 1978 Turbulent stage of the Rayleigh–Taylor instability. *Sov. Tech. Phys. Lett.* **4**, 299–300.

Kadau, K., Germann, T. C., Hadjiconstantinou, N. G., Lomdahl, P. S., Dimonte, G., Holian, B. L. & Alder, B. J. 2004 Nanohydrodynamics simulations: an atomistic view of the Rayleigh–Taylor instability. *Proc. Natl Acad. Sci.* **101**, 5851–5855.

Layzer, D. 1955 On the instability of superposed fluids in a gravitational field. *Astrophys. J.* **122**, 1–12.

Li, X. L., Jin, B. X. & Glimm, J. 1996 Numerical study for the three-dimensional Rayleigh–Taylor instability through the TVD/AC scheme and parallel computation. *J. Comput. Phys.* **126**, 343–355.

Linden, P. F., Redondo, J. M. & Youngs, D. L. 1994 Molecular mixing in Rayleigh–Taylor instability. *J. Fluid Mech.* **265**, 97–124.

Lindl, J. D. 1998 *Inertial Confinement Fusion: The Quest for Ignition and Energy Gain Using Indirect Drive*. AIP Press.

Miles, J. W. & Dienes, J. K. 1966 Taylor instability in a viscous liquid. *Phys. Fluids* 9, 2518–2519.

Patankar, S. V. 1972 *Numerical Heat Transfer and Fluid Flow*. Taylor and Francis.

Ramaprabhu, P. & Andrews, M. J. 2004 Experimental investigation of Rayleigh–Taylor mixing at small Atwood numbers. *J. Fluid Mech.* **502**, 233–271.

Read, K. I. 1984 Experimental investigation of turbulent mixing by Rayleigh–Taylor instability. *Physica* D **12**, 45–58.

Robinson, A. C. & Swegle, J. W. 1989 Acceleration instability in elastic–plastic solids. II. Analytical techniques. *J. Appl. Phys.* **66**, 2859–2872.

Schneider, M. B., Dimonte, G. & Remington, B. 1998 Large and small scale structure in Rayleigh–Taylor mixing. *Phys. Rev. Lett.* **80**, 3507–3510.

Scorer, R. S. 1957 Experiments on convection of isolated masses of buoyant fluid. *J. Fluid Mech.* **2**, 583–594.

Snider, D. M. & Andrews, M. J. 1994 Rayleigh–Taylor and shear driven mixing with an unstable thermal stratification. *Phys. Fluids* A **6**, 3324–3334.

Sohn, S.-I. 2003 Simple potential-flow model of Rayleigh–Taylor and Richtmeyer–Meshkov instabilities for all density ratios. *Phys. Rev.* E **67**, 26301.

Tennekes, H. & Lumley, J. L. 1972 *A First Course in Turbulence*. MIT Press.

Tryggvason, G. & Unverdi, S. O. 1990 Computations of three-dimensional Rayleigh–Taylor instability. *Phys. Fluids* A **2**, 656–659.

Van Leer, B. 1977 Towards the ultimate conservative difference scheme. IV. A new approach to numerical convection. *J. Comput. Phys.* **23**, 276–299.

Wilson, P. N. & Andrews, M. J. 2002 Spectral measurements of Rayleigh–Taylor mixing at low-Atwood number. *Phys. Fluids* A **14**, 938–945.

Young, Y. N., Tufo, H., Dubey, A. & Rosner, R. 2001 On the miscible Rayleigh–Taylor instability: two and three dimensions. *J. Fluid Mech.* **447**, 377–408.

Youngs, D. L. 1989 Modeling turbulent mixing by Rayleigh–Taylor instability. *Physica* D **37**, 270–287.

Youngs, D. L. 1991 Three-dimensional numerical simulation of turbulent mixing by Rayleigh–Taylor instability. *Phys. Fluids* A **3**, 1312–1320.

Youngs, D. L. 1994 Numerical simulation of Rayleigh–Taylor and Richtmeyer–Meshkov instabilities. *Lasers and Particle Beams* **12**, 725–750.

Youngs, D. L. 2003 Application of MILES to Rayleigh–Taylor and Richtmeyer–Meshkov mixing. *16th AIAA Comput. Fluid Dyn. Conf.* 23–26 June 2003. AIAA 2003-4102.